Wear 570 (2025) 206001

Contents lists available at ScienceDirect

Wear

journal homepage: www.elsevier.com/locate/wear

Importance of contact geometry for experimental tribological research of austenitic cast iron at high temperatures

Tobias König [a], Ziping Sang [a], Philipp Daum [a,b], Dominik Kürten [a], Andreas Kailer [a], Martin Dienwiebel [a,b,*]

[a] Fraunhofer Institute for Mechanics of Materials IWM, Microtribology Center μTC, Wöhlerstr. 11, Freiburg, 79108, Germany
[b] Institute for Applied Materials – Reliability and Microstructure at the Karlsruhe Institute of Technology, Straße Am Forum 7, Karlsruhe, 76131, Germany

ARTICLE INFO

Keywords:
Unlubricated contact system
Influence of contact geometry
Atmospheric effect
Third body
Glaze layer

ABSTRACT

This publication focuses on the influence of the contact geometry and especially the particle ejection on the tribological behaviour of unlubricated, thermally highly loaded contacts by a systematic comparison of a system and a model test. Moreover, the influence of temperature and the influence of an exhaust gas atmosphere on the tribological system behaviour of an austenitic cast iron was analysed in depth.

Between the system and model experiments, the dominant tribological mechanisms are broadly comparable, and the corresponding temperature regimes of the wear behaviour show excellent agreement. However, the wear rates and atmospheric effects are significantly different. By using grooved bushings, the influence of the particle ejection and thus the contact geometry on the tribological behaviour was analysed. For lower temperatures, comparable wear rates and atmospheric influences between the tests are only determined with grooved bushings.

1. Introduction

Tribological systems are highly complex, sensitive and are influenced by a variety of factors. Model experiments are often used for screening purposes to enable the relevant influencing factors to be easily varied as required. In the field of high-temperature tribology, where lubrication with conventional fluids is not possible, several contact geometries were commonly used. For fretting, two crossed cylinders with initial point contact [1–3] or a lying cylinder on a plate [4] are rubbed against each other. For reversing tests with higher displacements ball-on-disk [5] or lying cylinder-on-disk [6] contacts are established.

Alternatively, system test setups are specially designed to match the respective high temperature application and are therefore more complex. Components of variable stator vane systems (−40–600 °C) are for example tested with an application oriented, complex load spectrum [7] or the waste gate mechanism of internal combustion engines (up to 800 °C) [8] was replicated in an furnace. These application-related system tests always assume a high degree of transferability to the application. A lower transferability is usually attributed to the model tests, but this has only been verified in very few cases. Therefore, the question arises whether the higher transferability of the tribological results is indeed due to loading conditions which are closer to the application and identical machining of the samples or whether the used contact geometry also has a significant influence.

Our aim is to investigate the degree of transferability between a simple model test [6] and an application-oriented system test in the field of high-temperature tribology. The influence of temperature and atmosphere on the resulting wear behaviour and the dominant tribological mechanisms are analysed using the same material pairing. Finally, the influence of the contact geometry is investigated.

The application for this research are unlubricated plain bearings of control and regulating flaps, which are used in the exhaust gas system of internal combustion engines. They fulfil functions such as the demand-based inflow to different turbochargers, the regulation of the exhaust gas volume flow fed back into the intake system and, as brake flaps, increase the exhaust gas back pressure. These tribological systems are exposed to high temperatures, up to 850 °C for diesel engines [9] and are not sealed against the exhaust gas atmosphere.

The material pairing of an austenitic cast iron with a chromium-electroplated hot working steel derived from the application has already been tribologically characterised in depth with a cylinder-plate contact geometry. The temperature- and atmosphere-dependent results can be found in [6]. Further tribological investigations are rarely found for both materials in the targeted temperature range. Mottled

* Corresponding author.
E-mail addresses: tobias.koenig@iwm.fraunhofer.de (T. König), martin.dienwiebel@kit.edu (M. Dienwiebel).

https://doi.org/10.1016/j.wear.2025.206001
Received 18 September 2024; Received in revised form 14 February 2025; Accepted 17 February 2025
Available online 17 March 2025

cast iron was analysed by Zambrano et al. [10] at temperatures up to 600 °C. They found a wear-reducing oxide layer in the uppermost temperature range. The wear-reducing effect of chromium coatings has been demonstrated in some studies, at least at room temperature (RT) [11–13].

The dominant tribological mechanisms of unlubricated metal pairings are highly temperature-dependent, as Bowden et al. [14] have already highlighted. In the lower temperature range, adhesion through the bare material surfaces is dominant [15]. Above a material-specific temperature, oxidation wear sets in, which is characterised by flaking and abrasion of the oxide layer [16,17]. Some material pairings form a wear-reducing glaze layer at higher temperatures, which is created by the tribologically assisted agglomeration, compaction and sintering of oxidised wear particles [2,16,18–20]. With a further increase in temperature, this regime is replaced by high abrasive wear, which is determined by the hard, abrading oxide particles and the decreasing material strength [15].

Another important mechanism for an unlubricated tribological system is a so-called third body, first described by Godet [21,22], which is regarded as an intermediate phase in the tribo-contact and consists of wear particles. As these third bodies have load-carrying properties and separate the material surfaces of the contact partners, they may have friction and wear-reducing effects. The behaviour of the third body is a result of particle generation, entrapment, ejection and possible re-entry into the contact area [23,24]. As the contact geometry has a significant influence on the ejection in particular, differences between the experiments can be expected.

In addition, the atmosphere has a significant influence on the tribological mechanisms and thus the friction and wear behaviour. For example, in the model test [6], an atmosphere-induced decrease in wear was observed, which was explained by a lower oxidation of the graphite and the resulting lubricating effect. A change in the high temperature (HT) behaviour and the formation of the glaze layer was not detected at an oxygen content of approx. 5 vol.%, which is comparable to diesel exhaust gas from an internal combustion engine [25].

In contrast, in an almost oxygen-free helium atmosphere at temperatures of up to 950 °C, Rahaman et al. [26], found that a non-forming glaze layer leads to higher wear. Further atmospheric effects were only investigated at temperatures below 300 °C by Velkavrh et al. [27,28], Esteves et al. [29] and Qiu et al. [30]. They also observed an influence on the tribological behaviour with decreasing oxygen content, which is accompanied by decreasing oxidation. However, a shift of the tribochemical reactions due to changing gas components has a significantly stronger effect on the tribological behaviour than the oxygen level [27,28].

In the following, the influence of the atmosphere and the influence of temperature on a shaft-bushing contact system is analysed, which is similar to the application. Finally, the influence of the contact geometry is studied by using grooved bushings with increased particle ejection and a link is made to the model tests with the identical material pairing.

2. Materials and methods

2.1. Materials

For this research the same material pairing of former postulated model tests [6] were used. Therefore, the bushing is made of an austenitic cast iron and the chromium electroplated shaft consists of a hot working steel. Table 1 lists the composition of the studied materials. The microstructure of the materials is comparable to the visualised ones in [6]. The corresponding micro-sections after etching in a mixture of 3 vol.% nitric acid and 97 vol.% ethanol for 30 s are displayed in Fig. 1. On the shaft, the approx. 15 µm thick chromium layer is visible, as well as the fine pearlitic structure with an average grain size of 45 µm. The microstructure of the austenitic cast iron of the bushing shows spheroidal graphite with an average diameter of 29 µm which is interrupted by small and isolated pearlitic areas.

Table 1
Composition of the studied materials in wt.% [31,32].

Material	Fe	C	Cr	Ni	Si	Mn	Mo	V
GGG-NiCr-20–3 bushing	base	2.6	3	20	2.5	1	–	–
32CrMoV12–28 shaft	base	0.32	3	–	0.2	0.3	2.8	0.5

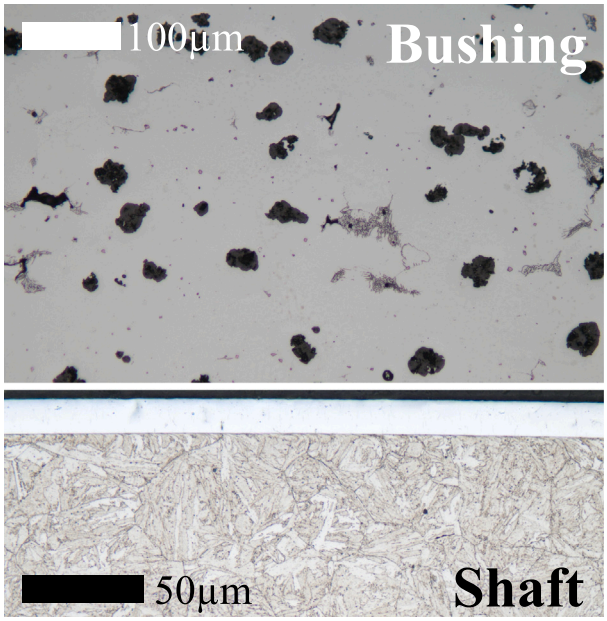

Fig. 1. Microstructure of the electroplated shaft and the cast iron bushing.

2.2. Tribological experiment

A dedicated test setup was developed at the Fraunhofer IWM within a publicly funded project[1] to enable application-oriented testing of thermally highly loaded, exhaust gas exposed and non-lubricated plain bearings. The testbench is shown in Fig. 2 and consists of a hydraulic normal force actuation (blue box), a heating chamber with the contact geometry (red box), an electric motor generating the oscillating rotation (green box) and an auxiliary heater for exhaust gas generation (yellow box). The centre of the test bench forms a shaft-bushing contact system with application-oriented dimensions of 14 mm shaft diameter and 15 mm bushing width, which is illustrated in Fig. 3. At a normal force (blue) of 240 N, which is pulling the bushing (orange) upwards by a hydraulic cylinder, an initial Hertzian pressure of 30 MPa is achieved. The shaft (red) is supported on both sides by grooved ball bearings and set into oscillation (δ) by a highly dynamic electric motor.

To record the wear development over time, the position sensor, a linear variable differential transformer (LVDT), of the hydraulic cylinder is used. The friction and rotational position of the tribological system is measured by a torque and rotational position sensor (burster präzisionsmesstechnik, Gernsbach Germany, type 8661-5050-V2400, ±0.05 Nm, 2000 increments per 360°), whereby the friction of the rolling bearings in the system is neglected. Similar to the model test, the calculation method of the energetic coefficient of friction ($ECoF$) is also used for this system test. Therefore, the dissipated energy of one friction cycle (E_d) is divided by four times the normal force (P) multiplied by the sliding amplitude (δ_0):

[1] IGF-project 21253; title: Characterisation of the wear of unlubricated tribological systems exposed to exhaust gases

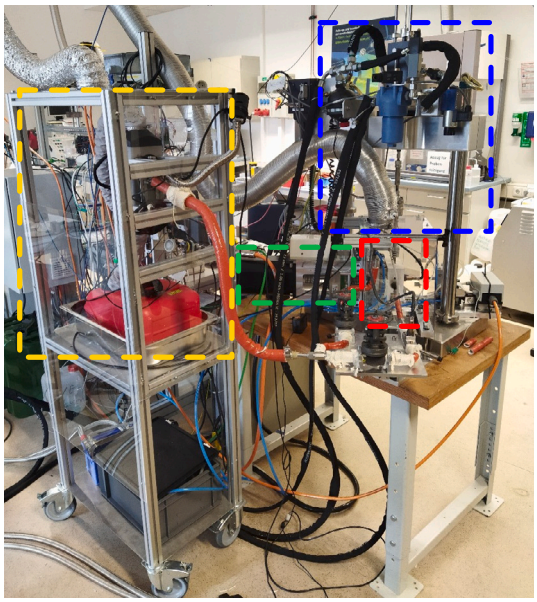

Fig. 2. Application oriented test bench for shaft-bushing contacts with exhaust gas admission; blue box: hydraulic normal force actuation, red box: heating chamber and contact geometry, green box: electric motor for oscillating rotation, yellow box: auxiliary heater for exhaust gas generation.

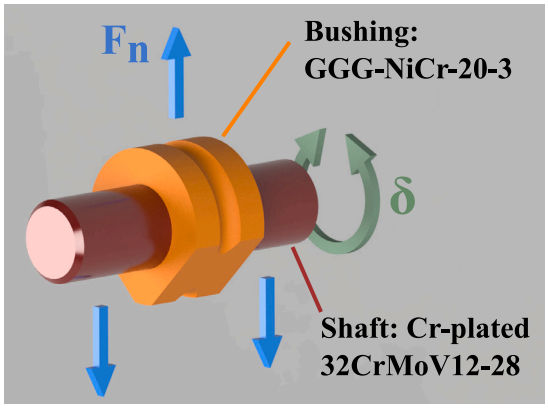

Fig. 3. Contact geometry with normal force F_n (blue) and rotational displacement δ (green): shaft-bushing.

$$ECoF = \frac{E_d}{4\ P\ \delta_0} \tag{1}$$

As shown elsewhere [1,33,34], this calculating method efficiently reduces the effect of wear-scar interaction on the coefficient of friction and allows results to be directly compared with other tribological experiments. Moreover, the calculation was accepted as a standard by the American Society for Testing and Materials [35].

In order to avoid high moments of inertia in the friction evaluation at frequencies of 15 Hz, which have to be applied for comparable test conditions to the model test, the system test procedure consists of two different frequencies. The first 120 cycles within one hour are carried out at a frequency of 1 Hz and the torque data are used to calculate the energetic friction coefficient. For the remaining 58 min, the shaft oscillates rotationally at approx. 15 Hz and an amplitude of 14.4°, leading to a rapid increase in wear without friction evaluation. The rotation by 14.4° corresponds to a sliding amplitude of 1.76 mm and is therefore comparable with the stroke of the model test of 1.6 mm.

Table 2
Test parameters of the tribological system experiments.

Parameter	Value	Unit
Load	240	N
Rotation angle	14.4	°
Frequency	1 & 15	Hz
Duration	19	h
Temperature	RT - 800	°C
Atmosphere	Ambient air, diesel exhaust gas (3.5 vol.% O_2)	

The test duration is in total 19 h which means that the shaft-bushing samples are exposed to approx. 1 million friction cycles.

A customised furnace chamber with two resistance heaters is used for the temperature control of the isothermal tests, which only heats the tribological contact bodies locally. A type *N* thermocouple is welded to the bushing for temperature measurement. Before starting the test, the contact bodies are thoroughly cleaned with isopropanol and brought to the target temperature with 7.5 K/min, whereby the last 20 K are heated at a slow heating rate of 1 K/min in order to achieve a homogeneous temperature distribution in the test setup and prevent thermal expansion during the test.

The heating chamber also has a heat-resistant oxygen sensor (Bosch LSU 4.9), which monitors the oxygen content near the tribological system. In addition, the burned combustion gas can flow through the heating chamber for tests in exhaust gas (approx. 3.5 vol.% O_2). To generate this gas a diesel auxiliary heater (Webasto Thermo & Comfort SE, Gilching Germany, Air Top 2000 STC Diesel 12 V) was used, which was located in a special designed and continuous aspirated box (Fig. 2 yellow box). Moreover, the exhaust gas leaking from the heating chamber was also aspirated, as well as the heated air of the auxiliary heater. By comparing the oxygen content directly after the auxiliary heater and in the furnace chamber, the atmospheric conditions at the tribological system are ensured, while increased fresh air leakage in the chamber is documented and leads to a failed test. The used oxygen sensors and the residual data recording systems were verified after a preheating time of 30 min in ambient air and with argon gas ($\leq$ 2 ppm O_2) and a maximum deviation of $\pm$0.02 vol.% O_2 was achieved after three alternating atmosphere tests. The temperature of the incoming exhaust gas is around 203 °C. For tests in exhaust gas, the tribological system is first heated to the target temperature before the auxiliary heater is started to generate exhaust gas. As soon as a constant exhaust gas temperature has been reached, the tribological test was started.

Table 2 summarises the test parameters, which are related to the conditions of the model tests described in [6]. They were defined within the previously mentioned IGF project in collaboration with the manufacturers of the components ensuring that the normal force, the sliding speed, the temperatures, and the atmosphere reflect the application as closely as possible.

For the tests with grooved bushings, a total of 18 grooves were eroded into the lower part of the bushing. This manufacturing process has the advantage that no undesired burrs occur at the edges of the grooves leading to increased contact stresses. The grooves were made at an average distance of 12°, with a width of 0.3 mm and at a right angle to the direction of movement (see Fig. 4), enabling the wear particles to be ejected once to the right and once to the left into a groove during each cycle, comparable to the model test. A depth of 1.5 mm was selected for the grooves in order to enable sufficient particle ejection even with larger wear depths.

2.3. Wear evaluation

The wear evaluation on the shafts was carried out in similarly as in our previous work [6] with a confocal microscope (confovis GmbH, Jena Germany, TOOLinspect Modell S) after cleaning with isopropanol. Using the structured illumination microscopy technique, a 1.28 mm

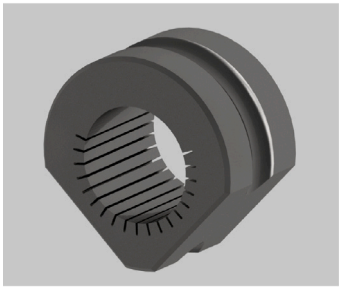

Fig. 4. Bushing with 18 grooves to promote particle ejection out of the tribological contact.

thick stripe was imaged across the entire width of the wear track with a height resolution of 0.3 µm. For this purpose, a position 25–35° next to the bottommost shaft position was selected. This position was chosen because the real line contact between the shaft and bushing is located here and therefore the highest wear of the contact pairing can be assumed. This phenomenon is shown in figure 1 in the supplementary data. The offset of the real line contact compared to the lowest shaft position, which can be regarded as the theoretical line contact, is due to the finite rigidity of the test setup. As a result of the friction force, the shaft moves minimally upwards on the bushing side wall and leads to a positional offset of the line contact to the left and right, depending on the direction of movement. For the wear calculation out of the confocal measurement, the tribologically unloaded zone next to the worn area was used to determine a reference height. This reference height was used to calculate the average wear depth and the average transfer height of the shafts.

It was necessary to use a 3-axis coordinate measuring machine (Hoffmann SE, München Germany, Garant MM2 CNC) to measure the bushings as concave surfaces are poorly suited for optical measuring methods due to the low reflection efficiency. With a resolution of approx. 0.1 µm in the X, Y and Z directions, a ball stylus with D = 1,981 mm, and a total of 180 touch points, the inner diameter of the bushing was measured at three heights after the tribological test, in the centre and 2 mm away from the outer edges in each case. The largest inner diameter measured in each case was averaged over the height and by subtracting the initial diameter the mean wear depth of the bushing was determined.

The following assumptions were made for the calculation of the wear volume: The wear distribution on the bushing and shaft lead to an elliptical shape with the radius (r_{bw}) respectively (r_{sw}), which at the ends of the semi-ellipse merges back into the original circular shape with (r_{b-ini}) respectively (r_{s-ini}). This simple assumption of elliptical wear formation, which does not require additional measurement of the contact bodies, has proven to be only partially correct. In most cases, a dent-like volume reduction occurred at the two turning points and only minimal wear at the lowest (theoretical contact) point.

The wear volume of the shaft (V_s) is calculated with the assumption of elliptical wear formation and with the width of the wear track (b_{sw}) from the confocal microscope images by:

$$V_s = \frac{\pi}{2}\,[r_{s-ini}^2 - r_{s-ini}\; r_{sw}]\; b_{sw} \tag{2}$$

The wear volume of the bushing (V_b) is calculated equivalently with a bushing width (b_{bw}) of 15 mm by:

$$V_b = \frac{\pi}{2}\,[r_{b-ini}\; r_{bw} - r_{b-ini}^2]\; b_{bw} \tag{3}$$

The corresponding CAD model was used to calculate the wear of the grooved bushings, which also allows a conversion between wear depth and wear volume. The previous assumptions regarding the elliptical wear shape and the transition between semi-ellipse and semicircle were retained. This procedure ensures that the grooves were taken into account in the calculation of the wear volume and therefore the test results are not falsified by them.

2.4. Characterisation of wear tracks

As a first step, before different characterisation methods were performed, the specimens were cleaned with isopropanol to remove loose wear particles. An digital single-lens reflex camera (Nikon, Tokjo Japan, DSLR D200) with a 60 mm macro lens and appropriate lighting technology was then used to take overview images of the worn surfaces of shaft and bushing.

To further investigate the tribological test specimen and determine the primary wear mechanisms, a scanning electron microscope (SEM) with a secondary electron detector (Carl Zeiss Microscopy, Oberkochen Germany, SUPRA™ 40VP) was utilised. Surface pictures were recorded using an acceleration voltage of 8 kV and a working distance of around 8 mm.

To investigate the tribochemical changes caused by temperature and atmospheric influences, X-ray photoelectron spectroscopy (XPS) was used on selected samples following additional cleaning with cyclohexane and isopropanol. XP spectra were collected using a PHI 5000 VersaProbe™ II (Physical Electronics Inc) and monochromatic Al Kα (1486.7 eV) X-rays. The constituent element depth profiles were measured using argon ion sputtering with a 200 µm spot size, 0.2 eV energy resolution, and 47 eV pass energy. The depth scale was calibrated using a SiO_2 wafer that had a predefined surface thickness. Typically, the samples were sputtered for 25 min at a rate of 2 nm/min (500 mA, 1 kV) in order to provide a detailed image of the surface chemical composition. After that, for the next 45 min, the sputter rate was raised to 10 nm/min (1000 mA, 2 kV), which produced an overall profile depth of 500 nm. XP spectra and depth profiles with LLS fitting were analysed by applying the PHI-Multipak software.

To identify different oxidation states of the oxides, Raman spectroscopy with a Renishaw inVia™ (Renishaw plc., Gloucestershire United Kingdom) was carried out on the cleaned wear surfaces. For this purpose, a 532 nm laser was operated at a laser power of approx. 0.8 mW and the surface was irradiated for a total of 90 s. The instrument-specific WiRE™ software was used to analyse the spectra and for automatic correction of the cosmic radiation.

3. Results

At first the tribological results of the standard bushings concerning the thermal and atmospheric effects are mentioned. The second subsection deals with the tribological results of the grooved bushings promoting debris ejection.

3.1. Tests with standard bushings

3.1.1. Influence of temperature

The diagram 5 shows the wear volumes of the shaft and bushing, as well as the energetic coefficient of friction for isothermal tests in air. A scatter bar represents the standard deviation of three independent tests. The hard chrome-plated shaft has a minimal, almost neglectable wear volume over nearly the entire temperature range tested here, except for 800 °C, where a slight increase in wear was detected. However, in order to evaluate the adhesive material transfer to the shaft, the increase in volume due to material transfer is shown as negative wear volume. This adhesive material transfer to the shaft increases slightly from RT to 200 °C and remains at a similar level up to 500 °C before returning to zero. The wear behaviour of the bushing can be described in two temperature ranges. In the lower temperature range between RT and 400 °C, the wear increases with higher temperature, has its highest value at 200 °C and then decreases again. Between 500 and

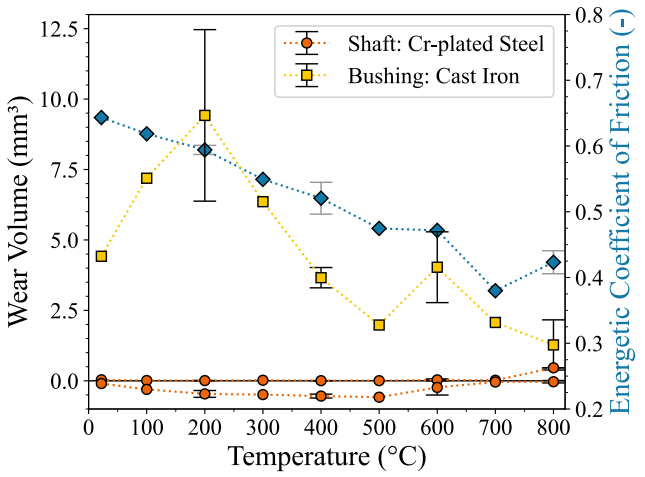

Fig. 5. Tribological results of isothermal system tests in air (240 N, 1 &15 Hz, 14.4°, 19 h), wear volume (mm³) of the shaft and bushing shown by orange circles and yellow cubes corresponds to the left axis, energetic coefficient of friction shown by blue diamonds corresponds to the right axis, markers represent the mean value and scatter bars the standard deviation of three independent tests.

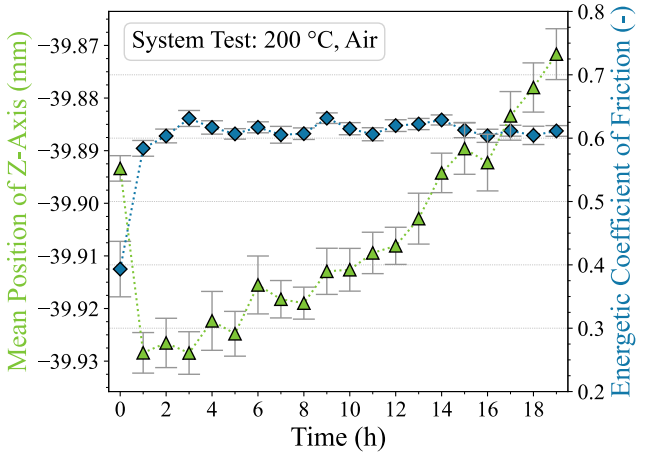

Fig. 6. Time dependent tribological material behaviour tested with a standard bushing at 200 °C in air (240 N, 1 &15 Hz, 14.4°, 19 h), *Z*-axis position of the hydraulic normal force cylinder [mm] shown by green triangles corresponds to the left axis, energetic coefficient of friction shown by blue diamonds corresponds to the right axis, markers represent the mean value and scatter bars the standard deviation of two-minute, high-resolution recording at different test times.

800 °C the wear values are consistently at a low level, only at 600 °C was slightly increased wear detected. The mean energetic coefficients of friction follow a slightly decreasing trend from 0.65 at RT to 0.46 at 600 °C. At 700 and 800 °C, however, the ECoF decreases to lower values between 0.38 and 0.42.

In addition to the friction and wear values averaged over the test time, it is also possible to analyse the corresponding time-dependent curves. These are shown for an exemplary test at 200 °C in air in Fig. 6. The test shows an initial, rapid increase in the ECoF during the first hour which then remains at a stable level of 0.61. The height position of the hydraulic normal force cylinder enables conclusions regarding the time-dependent wear development. The test starts at a height of −39.894mm during the first friction cycles and after one hour the position is declined to a height of −39.93mm, that gives a hint towards a formed particle bed as third body. In the remaining test period from 2 h onwards, an almost linear trend towards higher positions can be recognised, which corresponds to a continuous increase in wear.

For temperatures higher than 200 °C, no reliable evaluation of the position of the normal force cylinder is possible due to the low wear

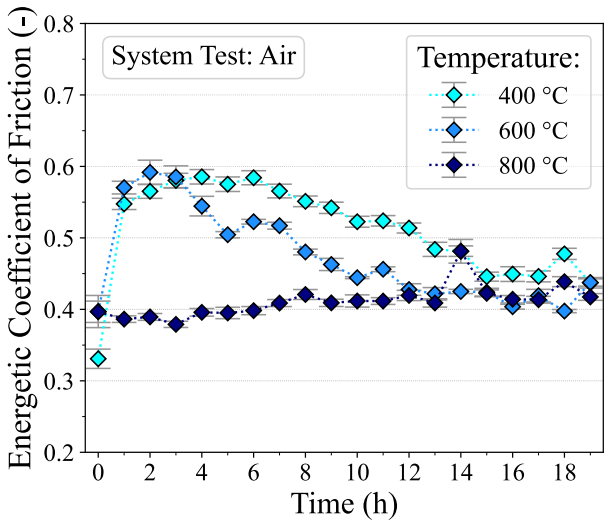

Fig. 7. Time dependent friction behaviour tested with standard bushings at 400, 600 & 800 °C in air (240 N, 1 &15 Hz, 14.4°, 19 h), energetic coefficient of friction shown by blue diamonds corresponds to the left axis, markers represent the mean value and scatter bars the standard deviation of two-minute, high-resolution recording at different test times.

depth combined with large thermal expansions, therefore the friction curves for 400, 600 & 800 °C are summarised in one Fig. 7. At 400 °C the initial friction behaviour is comparable to 200 °C, at first the ECoF rises to 0.55 and then remains at this high level. During the further progression of the test, from 6–8 h onwards, however, the behaviour differs from that at 200 °C, as the ECoF drops continuously to values of 0.44. This decrease in friction can also be seen in the friction behaviour at 600 °C, which starts after 3 h compared to 400 °C and reaches a slightly lower level of 0.41 after 12 h. The friction behaviour at 800 °C is in clear contrast to that at lower temperatures, as it already starts with an ECoF of 0.4 and maintains a constant, stable level around this value over the entire test.

To identify the dominant tribological mechanisms for the different temperature ranges, selected specimens were analysed using SEM. Fig. 8 shows the surface images of the wear scars of the bushings and Fig. 9 shows the wear scars of the shafts. The shown wear pattern are characteristic for the corresponding temperature range and serve as examples.

At 200 °C, the wear surface of the bushing is characterised by large, deformed, scale-like material adhesion and accumulated wear particles, which are interspersed in the direction of movement (vertically) by abrasive furrows of up to approx. 180 µm in width. At 400 °C, the large scales change into smaller ones, which are partially covered by an overlying, plastically deformed/smeared layer. Abrasive furrows still pervade the wear surface. With a further increase in temperature to 600 °C, large areas of the wear surface are dominated by a formed glaze layer, which is partially replaced by slightly deeper depressions with adhering wear particles. Abrasive marks are no longer visible at this temperature. The wear surface of the bushing at 800 °C is mainly characterised by strong oxidation and the resulting high surface roughness and island-shaped detachment of the oxide layer. Only isolated, darker and higher areas are identifiable, which show an overlay by a glaze layer.

The wear surface of the shaft at 200 °C clearly shows adhesive material transfer from the bushing, which is accompanied by many adhering wear particles. At 400 °C, the shaft is also covered with adhesive material transfer, which has a scale-like structure and, similar to the bushing, is partially covered by an overlying, plastically deformed layer. After a test at 600 °C, the shaft shows a glaze layer covering a large area, which was formed in the direction of movement and is

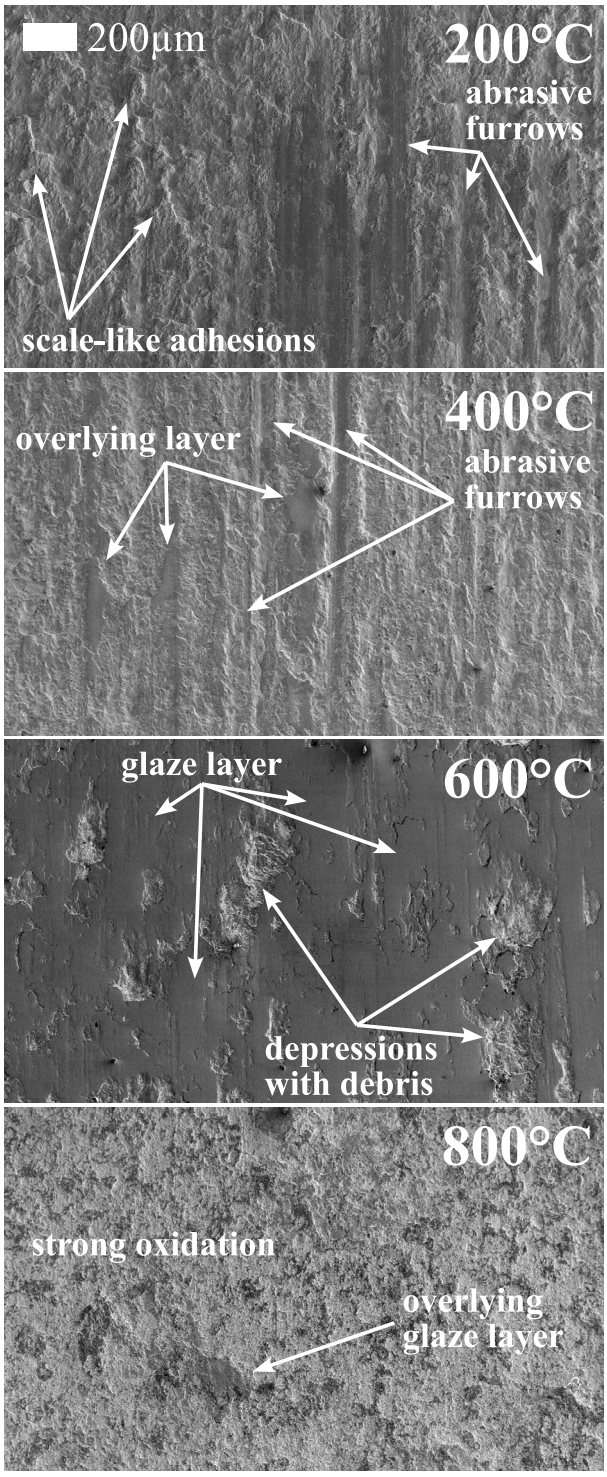

Fig. 8. Worn surface of standard bushings after isothermal tests at 200, 400, 600 & 800 °C in air; all images have the same scale.

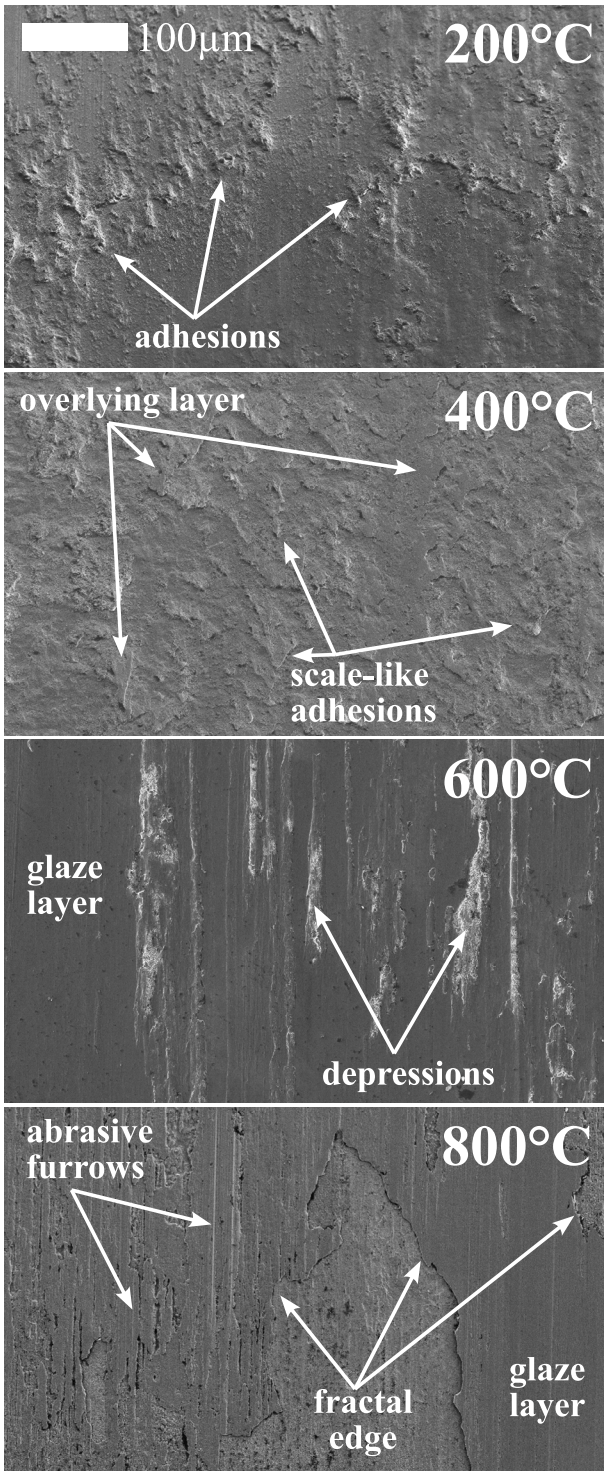

Fig. 9. Worn surface details of shafts after isothermal tests with standard bushings at 200, 400, 600 & 800 °C in air; all images have the same scale.

intersected by individual depressions or fractures. At 800 °C, the wear surface of the shaft is also characterised by a glaze layer with significant abrasive furrows as well as chipping and fracture edges of the layer.

Fig. 10 contrasts the wear surfaces of two shafts after tests at 200 and 600 °C, representing the two dominant tribological mechanisms of this material pairing. On the one hand, the brown, adhesive material transfer and wear particles from the bushing that adhere to the shaft at 200 °C. On the other hand, the tribologically formed glaze layer, shown here dark and highly reflective, which was built up on the shaft surface but does not fully cover the entire contact surface.

To evaluate the tribological impact on the base material and the structure of the glaze layer, a microstructural cross-section was made of a bushing tested at 700 °C, which is shown unetched in Fig. 11. A grown and adhering, darker oxide layer with a thickness of up to 27 µm is clearly visible on the material surface. This layer has several pores and consists in part of two areas with different colours. A transitional

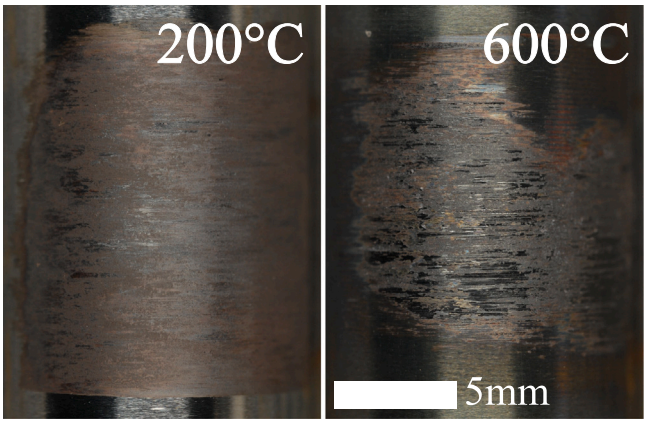

Fig. 10. Wear scar of shafts after isothermal tests with standard bushings at 200 & 600 °C in air; both images have the same scale.

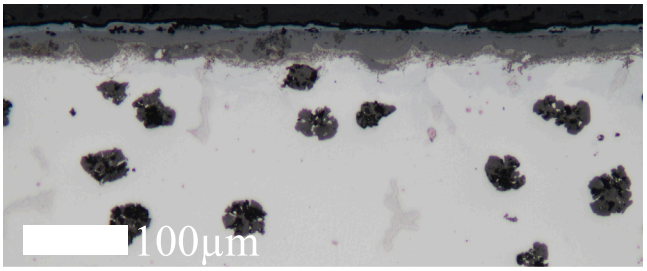

Fig. 11. Surface-near microstructure of a bushing tested at 700 °C in air.

area follows at increasing depth below the oxide layer, which has both oxidised, dark regions and lighter spots. Below a depth of 40 µm, the original material structure with spheroidal graphite is dominant.

In order to identify different oxidation states of the materials in the investigated temperature range up to 800 °C and to evaluate their effects on the tribological behaviour, the hard chromium-plated shafts were examined using Raman spectroscopy. The complete results in 100 K steps can be found in the supplementary data (figure 2). Only the results for samples after tests at 600 and 700 °C, which are representative of the temperature range below and above, respectively, are shown in Fig. 12 as extracts. The Raman spectra, which were measured at three different positions on the wear surface of the shaft after a test at 600 °C, uniformly show a large peak at 665 cm^{-1} and a slight peak at 300–320 cm^{-1}. These positions as well as the size relations of the peaks correspond to those of Fe_3O_4 (magnetite) [36]. Consequently, it is assumed that mainly Fe_3O_4 is formed in tribological contact at temperatures reaching up to 600 °C. A significantly different Raman spectrum was detected on the shaft after an experiment at 700 °C. A large peak can still be seen at 665 cm^{-1}, but a second one at 1320 cm^{-1}. Further small peaks are at 220, 300, 410, 500 and 610 cm^{-1}. However, these positions correlate with those of Fe_2O_3 (haematite) [37]. Nevertheless, as a large peak at 665 cm^{-1} continues to dominate, which has only a slight appearance in Fe_2O_3, it is assumed that the present oxide is a mixture of Fe_2O_3 and Fe_3O_4, causing the spectra to overlap.

To analyse the other chemical components of the material transfer, the third body and the glaze layer in more detail, XPS analyses were performed on both shafts and bushings in 200 K steps. The depth profiles of the sample bodies were summarised in two diagrams 13 by averaging the chemical proportions at a depth between 250 and 350 µm and plotting them over the corresponding test temperature. Unfortunately, the Fe2p3-peak was selected for the analyses on the shaft and bushing up to 600 °C, which is proven to be influenced by the nickel content [38,39]. Consequently, the measured iron contents up to 600 °C are of limited reliability.

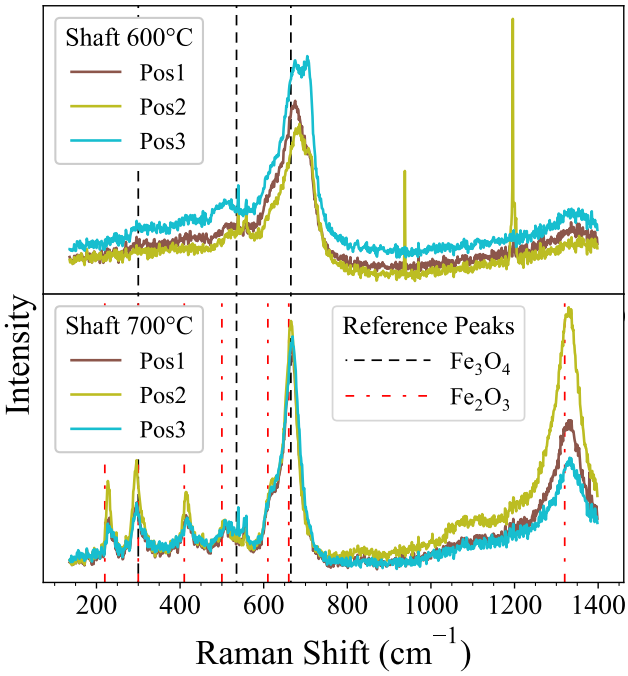

Fig. 12. Raman spectra from wear track of shafts at different positions after isothermal tests with standard bushings at 600 & 700 °C in air.

It is remarkable that the chemical composition of the adhering material transfer and of the glaze layer formed on the shaft does not change up to and including 600 °C. As only a minimal proportion of Cr and a significant proportion of Ni, as an alloying element that occurs exclusively in the bushing material, was detected, the material transfer to the shafts is also chemically proven. This material transfer consists of 49 at.% oxygen, approx. 28 at.% iron (possibly distorted), 15–18 at.% nickel and small amounts of silicon and carbon. In tests at 800 °C, the amount of chromium increases significantly, which is attributed to a not fully formed glaze layer, as a comparable amount of chromium was also measured on the top surface but also around the depth of 300 µm. In addition, the oxygen content increases significantly to 58 at.% and is accompanied by a decrease in the iron content to 22 at.%. This result supports the previously obtained findings from the Raman spectra indicating a change in the oxidation states from Fe_3O_4 to Fe_2O_3 above 600 °C. The proportion of nickel decreases at 800 °C to almost 0 at.%.

The chemical compositions near the surface of the bushing show a more complex, volatile temperature behaviour. The oxygen content increases slightly but constantly over the whole temperature range. This result confirms the previously discussed change in oxidation states from Fe_3O_4 to Fe_2O_3 above 600 °C, based on comparable iron amounts between 600–800 °C. The possibly distorted iron content fluctuates between 37 to 22 at.% in the temperature range up to 600 °C. The previously observed temperature-related decrease in the nickel content was also detected on the bushing. In particular, only a minimal proportion of nickel was measured at 600 °C, but even at 800 °C only 6 at.% was found. The carbon content, which reaches higher values in the temperature range between 200–600 °C, is mainly attributed to contaminations and solvent residues, which are particularly found in the porous adhered material and particle accumulations that occur in this temperature range. The low proportions of the additional alloying elements silicon and chromium show only slight changes for the different test temperatures.

3.1.2. Influence of atmosphere

This section presents the tribological results of the tests in exhaust gas atmosphere as well as subsequent analyses. Diagram 14 compares

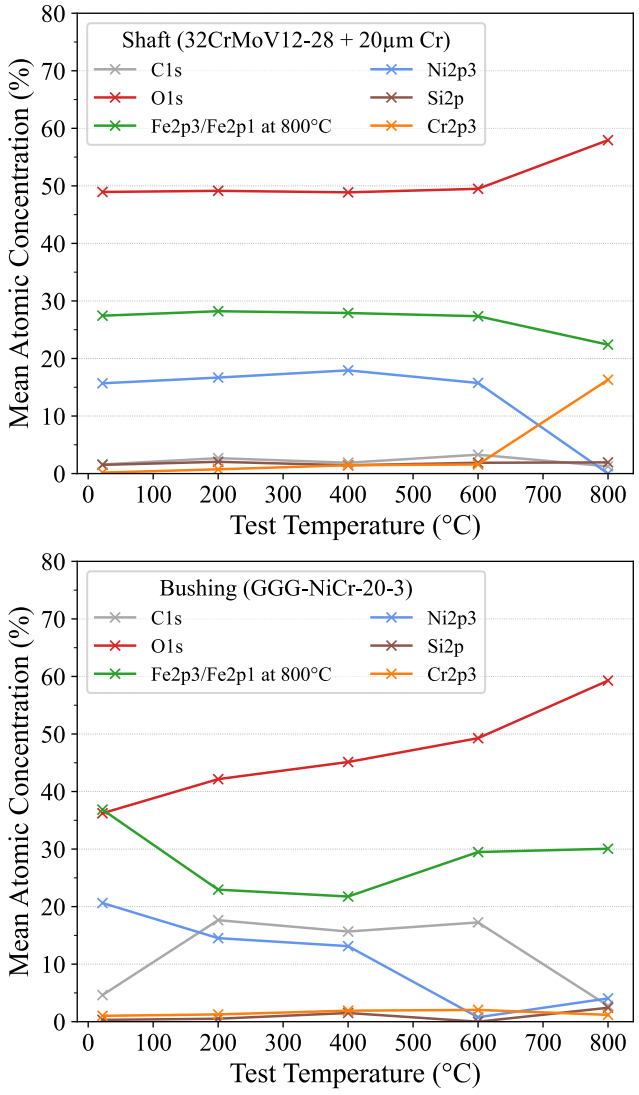

Fig. 13. Element concentration of XPS depth profiles at 300 nm over temperature for shafts and standard bushings tested in air (Fe2p3 possibly distorted by Ni).

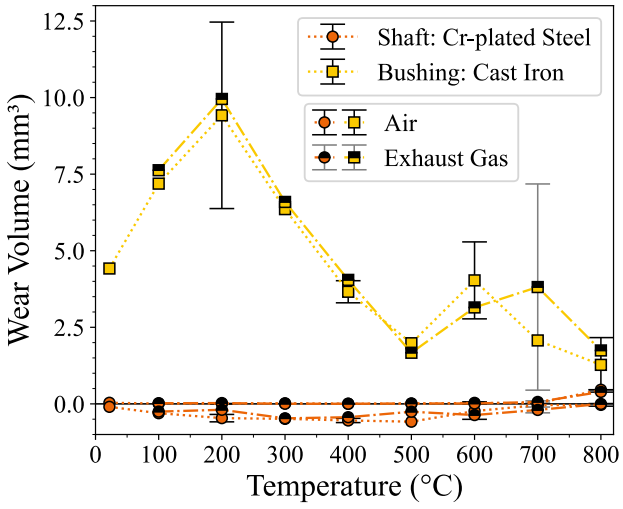

Fig. 14. Wear results of isothermal tests in air and exhaust gas atmosphere (240 N, 1 &15 Hz, 14.4°, 19 h), wear volume [mm³] of the shaft and bushing shown by orange circles and yellow cubes corresponds to the left axis, half-sided black markers indicate tests in exhaust gas, markers represent the mean value and scatter bars the standard deviation of three independent tests.

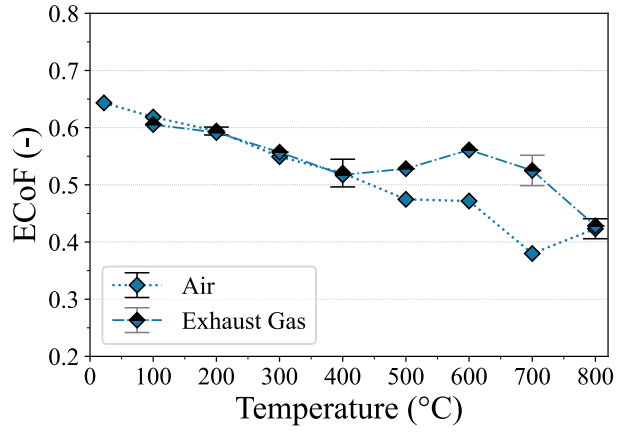

Fig. 15. Friction results of isothermal tests in air and exhaust gas atmosphere (240 N, 1 &15 Hz, 14.4°, 19 h), energetic coefficient of friction shown by blue diamonds corresponds to the left axis, markers represent the mean value and scatter bars the standard deviation of three independent tests.

the wear values marked with half-black markers and grey scatter bars from tests in exhaust gas with the values in air that have already been presented. No significant differences between the atmospheres can be seen up to and including 600 °C, the highest wear values were measured at 200 °C. Above 500 °C the wear is at a low level. Atmospheric wear differences only occur at 700 °C and above. Both the average wear of the bushing in exhaust gas is significantly higher than the value in air, and the standard deviation of the three tests in exhaust gas is significantly larger than that at 600 or 800 °C in air. This is attributable to a test that shows a very high wear value in the centre of the bushing, as a 0.5–1 mm area of material has chipped out of the bushing and adheres to the shaft. This phenomenon is shown in Figs. 17 and 18. In addition, two tests were aborted under these conditions as the bushing got stuck on the shaft and activated the torque limitation. Exceeded torque limit events did not occur under any other test conditions and are therefore not classified as normal behaviour of the contact pairing. Even at 800 °C, the wear in an exhaust gas atmosphere is slightly higher than in air and can be attributed to small material chipping on the bushing. This test in exhaust gas also had to be repeated because the shaft and bushing got stuck during the test.

The friction behaviour of the tests in exhaust gas is also indicated with half-sided black markers and compared with the results in air in Fig. 15. Similar to the wear behaviour, the friction behaviour in the lower temperature range up to 400 °C is not influenced by the exhaust gas atmosphere. Only between 500–700 °C a significantly higher friction level can be observed in exhaust gas than in air. At 800 °C, however, the low friction level of the tests in air is reproduced in exhaust gas.

For a more precise comparison of the friction differences between the atmospheres, the friction curves during the two-minute friction measurement at different test times are shown in Fig. 16. At the beginning of this exemplary selected test at 700 °C in an exhaust gas atmosphere, the ECoF starts at an unstable level of approx. 0.4 and reaches a very stable and constant level of 0.55 after 2–3 h, which persists for almost the entire remaining test time. However, there are two points in time, after 6 and 19 h, when the fluctuating friction deviates significantly from this stable behaviour and friction values of 0.67 are reached. Consequently, the increase in friction observed in the exhaust gas atmosphere is also accompanied by a significantly higher fluctuation of the ECoF over time, which is a characteristic of the observed adhesive material chipping.

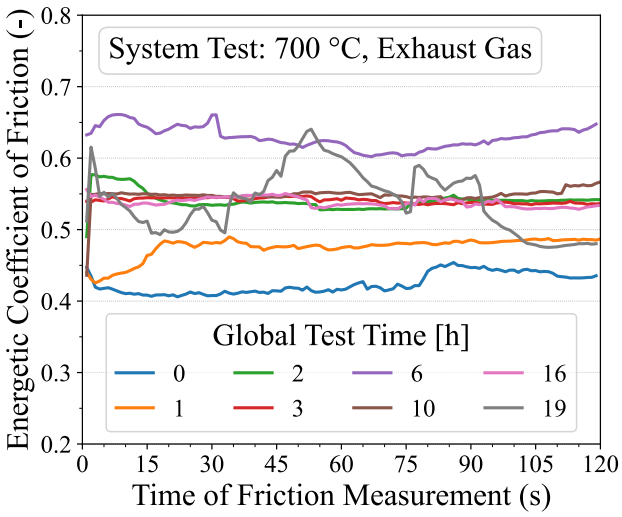

Fig. 16. Time dependent friction behaviour tested with a standard bushing at 700 °C in exhaust gas atmosphere (240 N, 1 &15 Hz, 14.4°, 19 h).

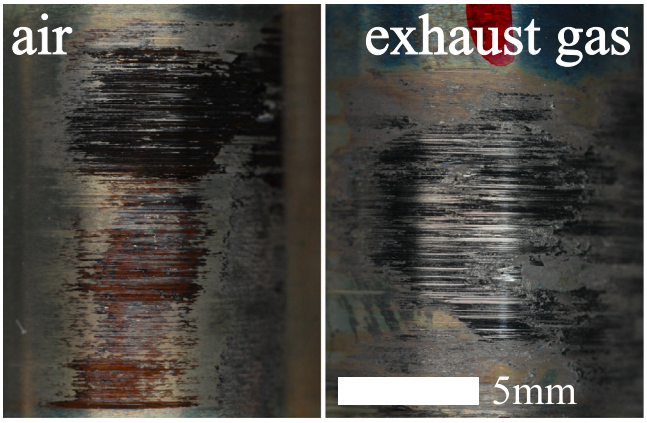

Fig. 17. Wear scar of shafts after isothermal tests with standard bushings at 700 °C in air & exhaust gas; both images have the same scale.

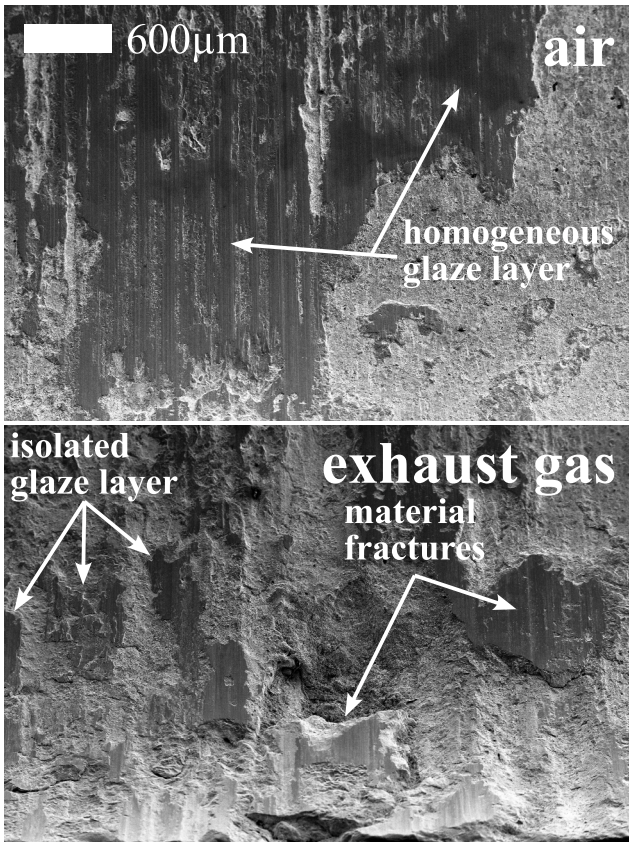

Fig. 18. Worn surface details of standard bushing after isothermal tests at 700 °C in air and exhaust gas; both images have the same scale.

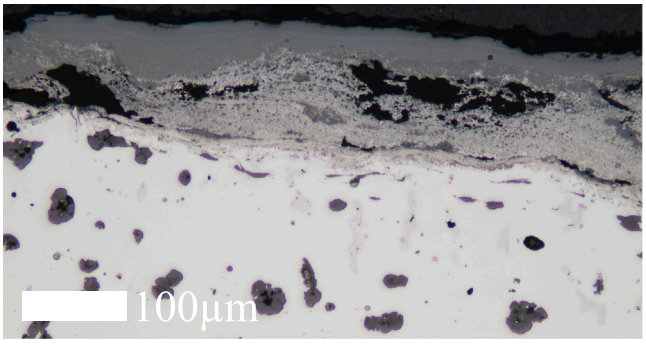

Fig. 19. Surface-near microstructure of a bushing tested at 700 °C in exhaust gas.

The adhesive material that fractures during exhaust gas tests at 700 °C are visualised in Figs. 17 and 18 for shaft and bushing with a macro and SEM image respectively. For comparison purposes, wear surfaces from tests in air are also shown. On the shaft, a significantly stronger abrasive grooving of the glaze layer in exhaust gas as well as large rough areas, partly with island-shaped adhesions, are visible. In contrast, the glaze layer in air shows a much more homogeneous appearance, with no adhesions or rough areas. In Fig. 18 of the bushings, these adhesive material chippings are clearly visible. The bushing in exhaust gas shows two 600–800 µm large fractured zones, which probably adhere elsewhere on the bushing surface again, are covered by a glaze layer and are accompanied by clearly observable furrows in the direction of movement that are up to 200 µm deep. Similarly, the remaining contact surface only shows a glaze layer at the higher areas. In contrast, the bushing from a test in air shows a uniform, continuous glaze layer surface, which is only occasionally disrupted by 50–80 µm wide furrows.

The microstructure of the unetched cross-section taken from a bushing tested in exhaust gas, shown in Fig. 19, differs significantly from that in air (Fig. 11). Here, an approx. 100 µm thick oxide layer is visible, which is twice as thick as in air. Different areas within the surface layer are also visible here, an upper, dark area with some pores and an underlying, light grey transition area with a large number of pores. Furthermore, in the adjacent base material, narrow, elongated graphite grains are visible, which indicate a strong plastic deformation of the material and thus also high loading.

Additional XPS depth profiles were measured at the contact bodies after a test at 700 °C in exhaust gas and shown in extracts for the shaft in Fig. 20. As a reference baseline, an XPS measurement of a shaft tested at 600 °C in air with possibly distorted iron content is used. On one hand, the test in exhaust gas showed a 4–5 at.% higher chromium content compared to air. This difference is attributed to the glaze layer, which does not completely cover the chromium coating of the shaft within the measuring spot of the XPS, whereby the composition of the layer is overlaid with the chromium coating. On the other hand, the depth composition in exhaust gas shows a slightly higher oxygen content and a lower amount of iron and nickel. These differences might either be due to a slight distortion of the results at 600 °C or are related to the atmospheric change.

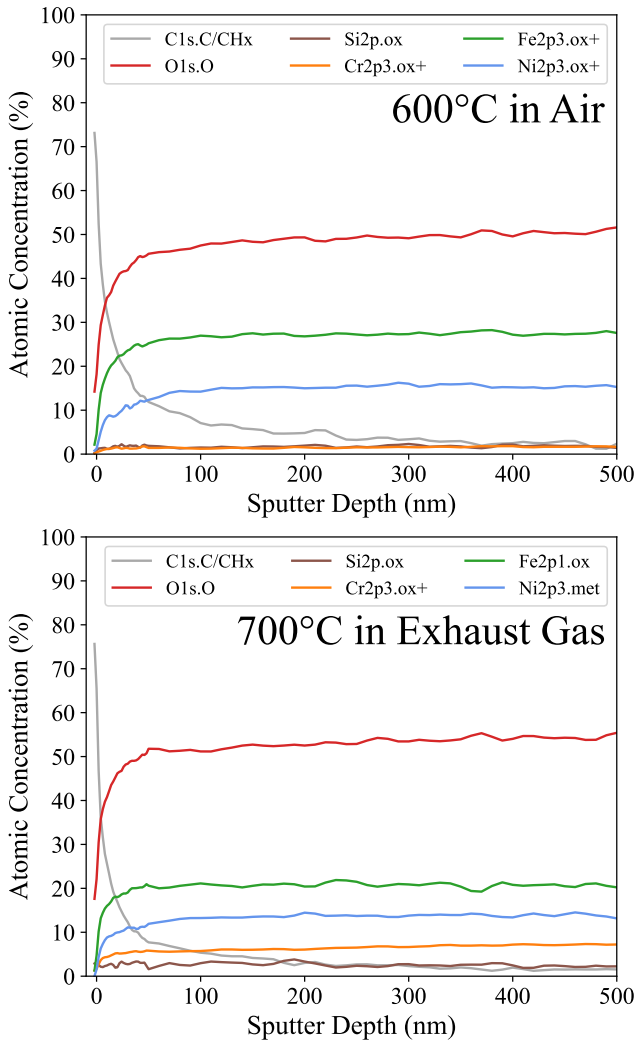

Fig. 20. XPS depth profiles of shafts after isothermal tests at 600 resp. 700 °C in air and exhaust gas.

Raman spectra, measured at different positions in the wear track of the shafts after the test at 700 °C, are provided in the supplementary data (figure 3). They show a comparable response to Fig. 12 (700 °C) and indicate the same oxidation state of the iron oxides as the experiments in air, consisting of a mixture of Fe_3O_4 and Fe_2O_3.

3.2. Tests with grooved bushings

To investigate the influence of the wear particles and a self-forming particle bed as a third body between contact partners, tests were carried out with grooved bushings. These tests were done at 200 °C, as the highest wear value with normal bushings were determined at this temperature and moreover, because an adhesive wear regime with high particle generation dominates here. In addition to tests in air, further tests were carried out in an atmosphere of exhaust gases to investigate the influence of the atmosphere on the changed contact geometry and possibly changed tribological mechanisms.

Fig. 21 depicts the wear and friction values determined with grooved bushings at 200 °C with those determined with normal bushings at 100–300 °C to highlight the difference between the contact geometry when compared to temperature changes. It clearly can be seen that there is a significant increase in wear on the bushing by a factor of five because of the grooves introduced, which is considerably higher than the temperature-related changes in wear. The minimum wear level of the shaft is not changed by the additional grooves in the bushing. However, the friction decreases slightly from a level of 0.59 with normal bushings to a level of 0.57 with grooves. In an exhaust atmosphere, the bushing wear decreases by 40% compared to air while the minimum shaft wear is not affected. This trend can only be observed with the grooved bushings; no atmosphere-related difference can be identified with the normal bushings. In addition to the reduction in wear with grooved bushings in an exhaust gas atmosphere, a further reduction in friction to a level of 0.55 was also recorded.

The development of wear and friction over time of an exemplary test with a grooved bushing at 200 °C in air is shown in Fig. 22. Initially low friction reaches a stable level of 0.55 after the first hour, which gradually rises to slightly higher values around 0.6 during the rest of the test. Furthermore, an almost linear increase of the z-position of the hydraulic normal force cylinder and therefore a linear increase in wear was recorded over the test time.

To compare the dominant tribological mechanisms between the tests with standard bushings and grooved bushings, the wear surfaces are depicted at two different magnifications in Fig. 23. The top two images show the normal bushings, which are characterised by 100–200 µm wide furrows in the direction of movement, large, scale-like deformed material particles on the surface and accumulated wear particles. At higher magnification, the adhering particles in particular, but also abrasive marks at the bottom of the furrows, are clearly identified. The two lower images were taken of the grooved bushings. The furrows are clearly visible at low magnification but are reduced in size compared to the initial state due to plastic deformation of the bushing material. A slightly different wear pattern is visible here; the surface is still characterised by abrasive furrows and slight plastic deformations, but these are significantly narrower (15–20 µm) and appear less deep. Furthermore, only small adhering wear particles can be seen, which no longer have a scale-like shape and generally seem to be less present. When comparing the material transfer adhering to the chrome plating of the shafts (see supplementary data figure 4), it is evident that the transfer is characterised by significantly smaller particles and stronger smearing/plastic deformation in the case of grooved bushings.

The grooved bushings tested in an exhaust gas atmosphere (supplementary data figure 5) show a comparable wear pattern to the bushings tested in air shown in Fig. 23. An abrasive but narrow grooving is accompanied by sporadic, adhering and deformed small wear particles. The shafts tested in an exhaust gas atmosphere show adhering material transfer, similar to the tests in air.

To analyse the atmospheric wear reduction in exhaust gas in more detail, XPS depth profiles were determined on the samples with grooved bushings. Selected results of the grooved bushing in exhaust gas are compared with a normal bushing in air in Fig. 24, both were tested at 200 °C. The major difference between the measurements is obvious: with a normal bushing in air, a tribologically mixed and oxidised layer forms on the material surface, which extends further into the base material than the measuring range of 500 nm used. With the grooved bushing in exhaust gas, this oxidised area can only be detected at a depth of 50 nm. At greater depths, the composition of the bushing material dominates. In addition to the oxidation depths, another difference can be seen by analysing the results in more detail: the depth profiles of the carbon content are different. In air, there is a near-surface maximum of 58 at.%, after 100 nm the carbon content drops to 23 at.% and at a depth of 500 nm it is 16 at.%. The grooved bushing tested in exhaust gas starts at 61 at.% carbon at the surface, after 100 nm it still has a quantity of 30 at.% and at 500 nm depth it has a content of 25 at.%. This distinctive increase in the carbon content is attributed to the different atmospheres.

4. Discussion

4.1. Discussion of shaft bushing results

The tribological high-temperature behaviour of the investigated material pairing consisting of a chromium-plated hot-work tool steel

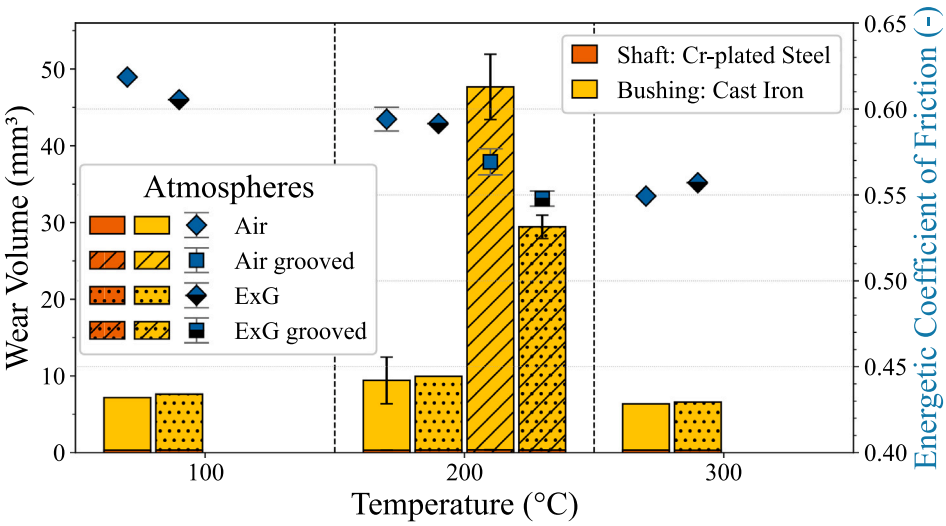

Fig. 21. Tribological results of isothermal tests with grooved bushings in air and exhaust gas atmosphere (240 N, 1 &15 Hz, 14.4°, 19 h), wear volume [mm³] of the shaft and bushing shown by orange and yellow bars corresponds to the left axis, energetic coefficient of friction shown by blue diamonds corresponds to the right axis, markers or bars represent the mean value and scatter bars the standard deviation of three independent tests.

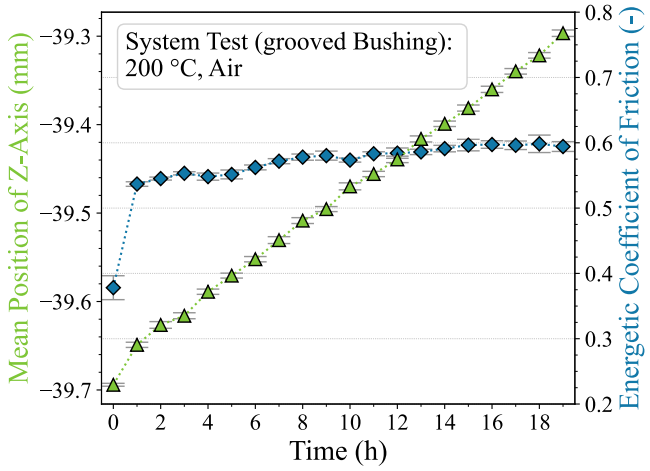

Fig. 22. Time dependent tribological material behaviour tested with a grooved bushing at 200 °C in air (240 N, 1 &15 Hz, 14.4°, 19 h), *Z*-axis position of the hydraulic normal force cylinder [mm] shown by green triangles corresponds to the left axis, energetic coefficient of friction shown by blue diamonds corresponds to the right axis, markers represent the mean value and scatter bars the standard deviation of two-minute, high-resolution recording at different test times.

and an austenitic cast iron can be divided into two temperature ranges. Between RT and 400 °C, the wear behaviour is dominated by a particle bed as third body separating the contact bodies. In this temperature range, the wear initially increases and reaches its maximum at 200 °C. This increase might be attributed to a thermally enhanced oxidation, which, comparable to the wear model of Quinn [17], leads to higher wear due to flaking of oxide layers. As the temperature continues to rise, the wear decreases as a result of possibly changed states of motion or adhesion tendencies within the third body. Material transfer from the bushing can be found on the generally unworn chrome layer of the shaft (Fig. 9 & 13). The bushing itself is characterised by flaky material adhesions and wide abrasive furrows (Fig. 8) and shows the highest wear in this temperature range. The material surfaces and therefore also the wear particles are present here in an oxidised state as Fe_3O_4 (Fig. 12), whereby the oxide content increases with temperature (Fig. 13). The developed third body was verified by the position signal of the hydraulic normal force cylinder (Fig. 6), as it moved downward after the first hour and the formation of the third body instead of moving upward, which would be expected in the case of wear or settling. This height difference of 36 µm is therefore attributed to the formation of a third body. In this wear region, the wear increases linearly with time and the friction is between 0.65–0.5 with a constant time behaviour (Fig. 7).

In the upper temperature range from 500 °C to 800 °C, a glaze layer is formed, which leads to a significant reduction in friction and wear (Fig. 5). The wear surfaces of the contact bodies are not completely covered at any temperature, at 600 °C depressions with adhering abrasion are visible and at 800 °C abrasive furrows penetrate the glaze layer on the shaft (Fig. 9). At 800 °C the bushing is already above the thermal limit and shows strong oxidation (Fig. 8). It has been proven that starting at 700 °C the glaze layer consists of a mixture of Fe_3O_4 and Fe_2O_3 (Fig. 12), which correlates with an already initially low and stable coefficient of friction (Fig. 7). At 500–600 °C, however, the glaze layer consists mainly of Fe_3O_4 and shows higher coefficients of friction of up to 0.6, which only reach a stable level of around 0.4 in the further progress of the test. Based on this, it is assumed that these differences in oxidation states are responsible for the different friction properties.

The lower temperature range dominated by the third body is not influenced by a change in the surrounding atmosphere from air to diesel exhaust gas. This is attributed to the separating but gas-permeable layer of debris and the residual oxygen content that is still present in the exhaust gas. As a result, the tribological system can continue to react with oxygen at any point, produce oxidised surfaces and particles and form the same tribological mechanisms as in air.

In the upper temperature range characterised by the glaze layer and especially at 700 °C, a significant change can be identified due to the atmospheric variation. On the one hand, significantly higher coefficients of friction are observed, which are accompanied by a volatile time behaviour. On the other hand, there are large adhesive chippings on the bushing, which in some cases still adhere to the shaft and are overlaid by a glaze layer in some areas. Furthermore, a thicker oxide layer was detected in the exhaust gas atmosphere, which is accompanied by a highly porous transition layer. It is therefore possible that stronger oxidation or corrosion occurs in the exhaust gas, which leads to the instability of the oxide layer and thus explains the increased adhesive material transfer. The chemical analyses (Raman and XPS) show no clear atmospheric differences, which means that the change in tribological behaviour cannot be explained by different chemical compositions. Consequently, the question concerning the cause of the

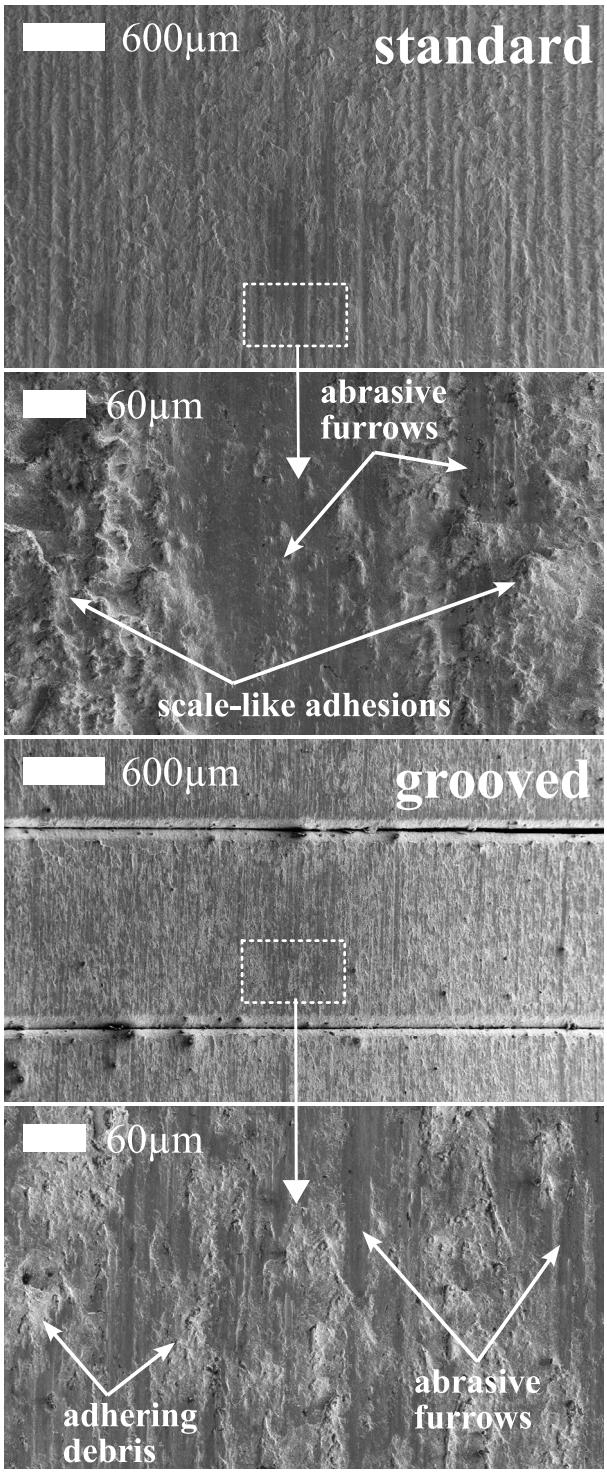

Fig. 23. Worn surface details of standard bushing and grooved bushing after isothermal tests at 200 °C in air.

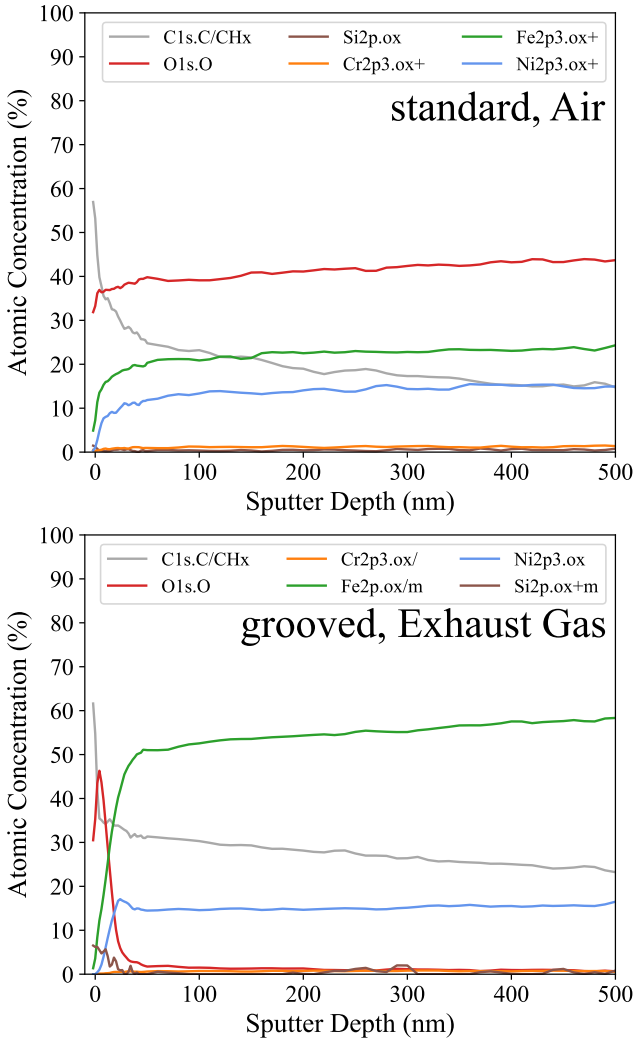

Fig. 24. XPS depth profiles of standard bushings tested in air and grooved bushings tested in exhaust gas, both at 200 °C.

atmosphere-induced change in wear cannot be fully answered and requires further investigation.

The tests with grooved bushings definitively demonstrated the important role of the third body in the wear behaviour of this material pairing. The grooves in the contact surface, which make it easy for wear particles to be ejected, increase wear by a factor of five compared to normal bushings. Furthermore, no change in the normal force cylinder position was determined for the grooved bushings (Fig. 22). In addition, a comparison of the contact surfaces of the bushings shows that no large flake-like material adhesions and wide abrasive furrows dominate, which are produced by agglomeration and deformation of the debris in normal bushings. Instead, the small, oxidised, individual wear particles are removed directly from the contact area, leaving mainly narrow abrasive furrows on the surface of the bushing. Accordingly, the low oxide layer thickness in the XPS results (Fig. 24) can be explained, as no oxidised and agglomerated wear particles from the third body are incorporated into the bushing surface with grooved bushings. Consequently, the mechanism of the third body was specifically prevented by the grooved contact geometry and the corresponding wear behaviour was shifted towards abrasion.

Interestingly, the tribological system with a grooved bushing reacts significantly to the change of surrounding atmosphere, whereas normal bushings show no difference. In exhaust gas, the wear of the grooved bushing decreases significantly and is accompanied by a slight reduction in the coefficient of friction. Based on the XPS results, which show an increase in the carbon content in the area near the surface, it is assumed that the graphite present in the material and the soot introduced by the exhaust gas acts as a lubricating medium. Particularly in the abrasive wear mechanism of the grooved bushings, the carbon can develop its wear and friction-reducing effect through the formation of an amorphous carbon layer [40]. In normal bushings, the relative movement of the contact bodies mainly takes place through rolling of

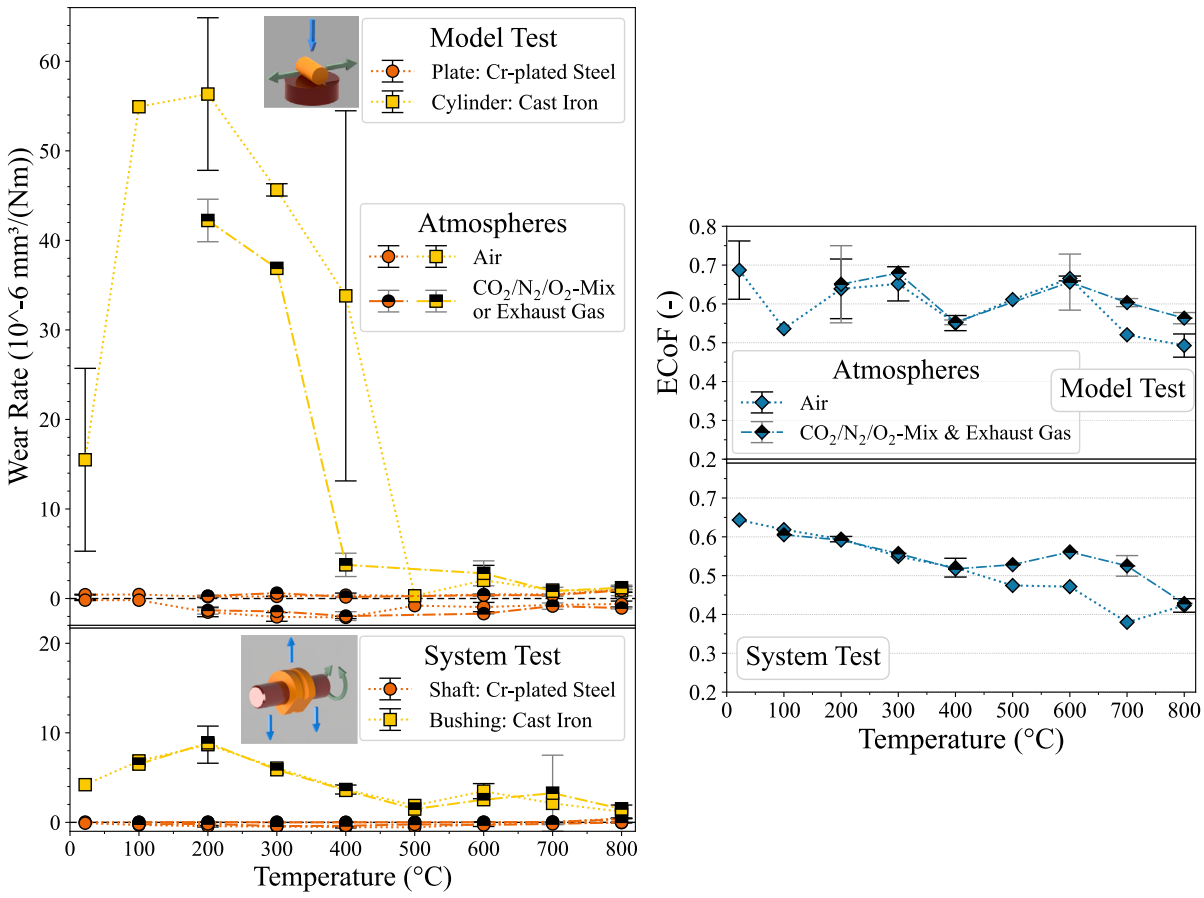

Fig. 25. Comparison of tribological results between system test and already published model test [6], wear rate [10^{-6} mm^3/(Nm)] of the shaft/plate and bushing/cylinder shown by orange circles and yellow cubes in the left diagram, energetic coefficient of friction shown by blue diamonds corresponds to the right diagram, markers represent the mean value and scatter bars the standard deviation of three independent tests.

the wear particles in the third body. A higher carbon content and its lubricating effect have only a minimal influence on this. This finding confirms the important role of the third body as a wear mechanism and guarantees an atmosphere-independent wear behaviour with low wear rates in the application.

4.2. Comparison with model test

The discussed results were generated using a self-developed test setup that optimally reproduces the load conditions and contact geometries of the application. The same material pairing has already been tribologically characterised in depth with a model test and published in [6]. The following discussion focuses on how a change in the contact geometry and individual load conditions affects the tribological material behaviour.

Diagram 25 compares the wear and friction values of the system test with those of the model test from [6]. Due to different test durations and normal forces, wear rates are shown instead of wear volumes.

When comparing the wear rates quantitatively, the wear level of the model test is six times higher. There are two factors that differ between the tests and are potentially responsible for the different wear levels. On the one hand, significantly different contact pressures occur (initial Hertzian pressure: model experiment: 174 MPa at 50 N; system experiment: 30 MPa at 240 N), which are not compensated by the different normal forces in the calculation of the wear rates. On the other hand, the contact geometries differ: in the model experiment, the circumferential surface of a cylinder is in contact with a plate, while in the system experiment a shaft rotates in a bushing. Therefore, an open contact geometry in the model experiment contrasts with a closed contact geometry in the system experiment, which could influence the interaction with the surrounding atmosphere. The geometries also result in different scenarios for the ejection of wear particles out of the contact area, which is an important influencing factor according to [22]. With the open model geometry, an ejection of wear particles is particularly likely in the direction of movement, as the contact area is very small compared to the stroke, and it is also not realistic for the particles to re-enter the contact zone. However, ejection is also possible perpendicular to the direction of movement. Although the closed system geometry allows particles to be ejected in the direction of movement, the circular shape of the bushing is likely to keep the particles in the contact zone due to gravity. Consequently, final and complete particle ejection is only possible at perpendicular to the movement, i.e. at the faces of the bushing.

When qualitatively comparing the wear behaviour over temperature, the results of both test methods are comparable. At room temperature the wear is at a medium level, between 100 and 400 °C a severe wear regime occurs with a maximum at 200 °C and above 500 °C the wear reaches a minimum level due to the formation of a glaze layer. The temperature-dependent mechanism changes are therefore comparable for both experiments. However, the influence of the atmosphere on the wear is different. The model experiment shows slightly lower wear values for the severe wear range (100 to 400 °C) in a $CO_2/N_2/O_2$-atmosphere compared to air; no differences between the exhaust gas atmosphere and air were observed for the system experiment. However, in the high temperature range at 700 °C, the system experiment in exhaust gas leads to a jamming of the shafts due to adhesion, accompanied by higher wear. This phenomenon was not observed in the model experiment.

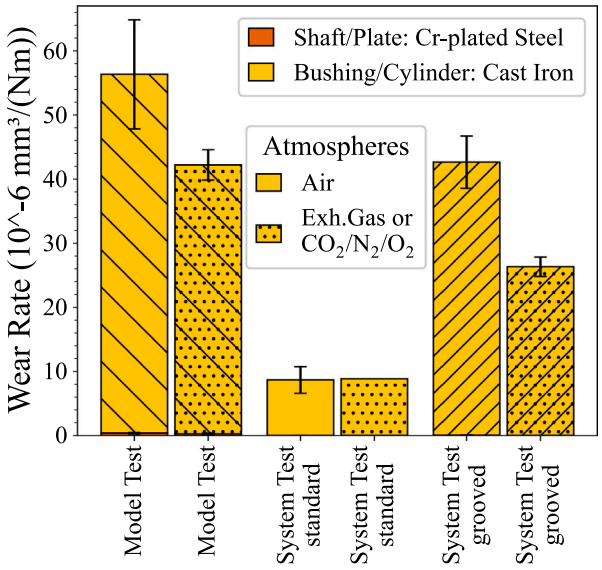

Fig. 26. Wear rate of grooved bushings at 200 °C in comparison with standard ones in the system test and already published results of the model test [6], wear volume [mm³] of the shaft and bushing shown by orange and yellow bars, bars represent the mean value and scatter bars the standard deviation of three independent tests.

In addition to the comparison of the wear values, the tribological mechanisms dominating in the respective temperature range should also be regarded. At low temperatures around 200 °C, adhesive material transfer to the hard chrome-plated contact bodies is dominant for both experiments. The cast cylinder of the model test shows abrasive furrows and sporadically adhering oxidised debris. In contrast, the wear surface of the cast bushing is characterised by a higher amount of adhering wear particles, which appear to be plastically deformed and form scale-like structures. The wear mechanisms at 400 °C are basically comparable to those at 200 °C, the adhering wear particles on the bushing and cylinder show more layer-like structures. At 600 °C, a glaze layer is present on all contact bodies, although it is significantly more homogeneous and more extensive in the system experiments than in the model experiments. A glaze layer also forms in the experiments at 800 °C. The cast bushing of the system test is strongly impacted by the onset of oxidation. The cast cylinder of the model test shows this behaviour less clearly, whereby it is not heated directly and reaches slightly lower temperatures.

The frictional behaviour differs significantly between the two experiments, although the same method of calculating the energetic coefficient of friction was used. Only the decrease starting at 700 °C due to the formation of Fe_2O_3 in addition to Fe_3O_4 is comparable for both experiments.

Accordingly, the results show no direct correlation between the model and system experiment. To investigate the question whether the different pressures or the different particle ejection conditions lead to the previously discussed differences between the experiments, the results of the grooved bushings are now included in the discussion. For this purpose, the wear rates at 200 °C under different atmospheres for the model experiment, the normal system experiment and the system experiment with grooved bushings are compared in Fig. 26.

Wear rates were determined with grooved bushings that are close to the level of the model experiment. A specific amount of the wear volume of the grooved bushing is certainly caused by the plastic deformation and dislocation movement due to the shear forces, which demonstrably lead to a narrowing of the grooves. However, it should be highlighted that the wear mechanisms between the experiments are significantly aligned. There are no scale-like structures due to adhering and plastically deformed particle agglomerations visible on the grooved bushings; only a slight adhesion of debris dominates comparable to the model experiment. Furthermore, with grooved bushings, the same atmospheric effect as with the model experiment can be observed with a reduction in wear. The lower oxidation of the graphite that is present in the material and the possible presence of soot supports their friction and wear-reducing effect for dry material contacts.

Due to the identical wear mechanisms, a comparable atmospheric influence and higher wear rates for the model experiment and the system experiment with grooved bushings, the non-forming third body is assigned a significant role as a wear mechanism. This particle bed as third body only occurs in the system experiment with normal bushings, where the geometry hinders particle ejection. Following this, the contact geometry and, especially, the ejection and re-entry probability of wear particles is a significantly important influencing factor for unlubricated, tribological systems. The different contact pressures between the experiments only have a subordinate role as an influencing factor. The geometry-based differences and the corresponding dominant wear mechanisms are summarised schematically in Fig. 27.

Consequently, it can be stated that the determined wear rates and the atmospheric influences between the model experiment and the system experiment do not directly correlate, due to different tribological mechanisms. The low temperature regime of the model experiment is characterised by light abrasion whereas the system experiment builds a particle bed as third body. With a higher particle ejection due to a grooved system contact, it was shown that the third body was effectively prevented, leading to transferable wear mechanisms and atmospheric influences to those of the model test. Both initial experiments are only comparable in the high temperature regime, where the formation of the glaze layer dominates.

4.3. Integration into the scientific context

The wear-reducing effect of third bodies on unlubricated contacts has already been demonstrated in many publications [41–46], and the resulting particle beds have also been analysed in detail in some cases. For example, Gasser et al. in [47] determined a decrease in wear with increasing thickness of the third body. The reduction in wear was attributed to a change in particle movement, as the increasing thickness of the particle bed results in an enhanced rolling movement of the abrasive particles. However, wear also decreases due to the reduction of direct interaction between particles and contact surfaces by a third body [48]. Furthermore, the shear force acting on the material surfaces is also reduced by a third body, as localisation occurs in the third body [45,49]. This effect also reduces wear. The addition of oxide particles consisting of Fe_2O_3 and Fe_3O_4 to the contact system also led to a reduction in the wear level [50], with comparable results being obtained for both oxidation states.

The interaction of the particles within the third body also influences the wear mechanism and rate. Depending on the particle cohesion, granular accumulations, particle compaction or plastically deformed material deposition can occur and cause different degrees and depths of stress in the base material [51–53]. However, the particle shape and size also influence the interaction within the third body and thus the wear [43]. In the context of particle size, some studies [42,54,55] report a mutual dependence with surface roughness. The theory was developed that if there is a large size difference between particles and asperities, the small particles are easily trapped by the roughness peaks. However, the contact-separating effect of the particles increases with their size, which means that the particles must be larger than the asperities for effective wear reduction.

The influence of different contact areas on the formation of a third body has already been investigated in several studies [1,42,56]. A decrease in wear rates was observed with a larger contact area and explained by the decrease in particle ejection. In addition to the contact area, the geometry also has an influence on the third body. In open contact systems, re-entry into the contact zone rarely occurs after

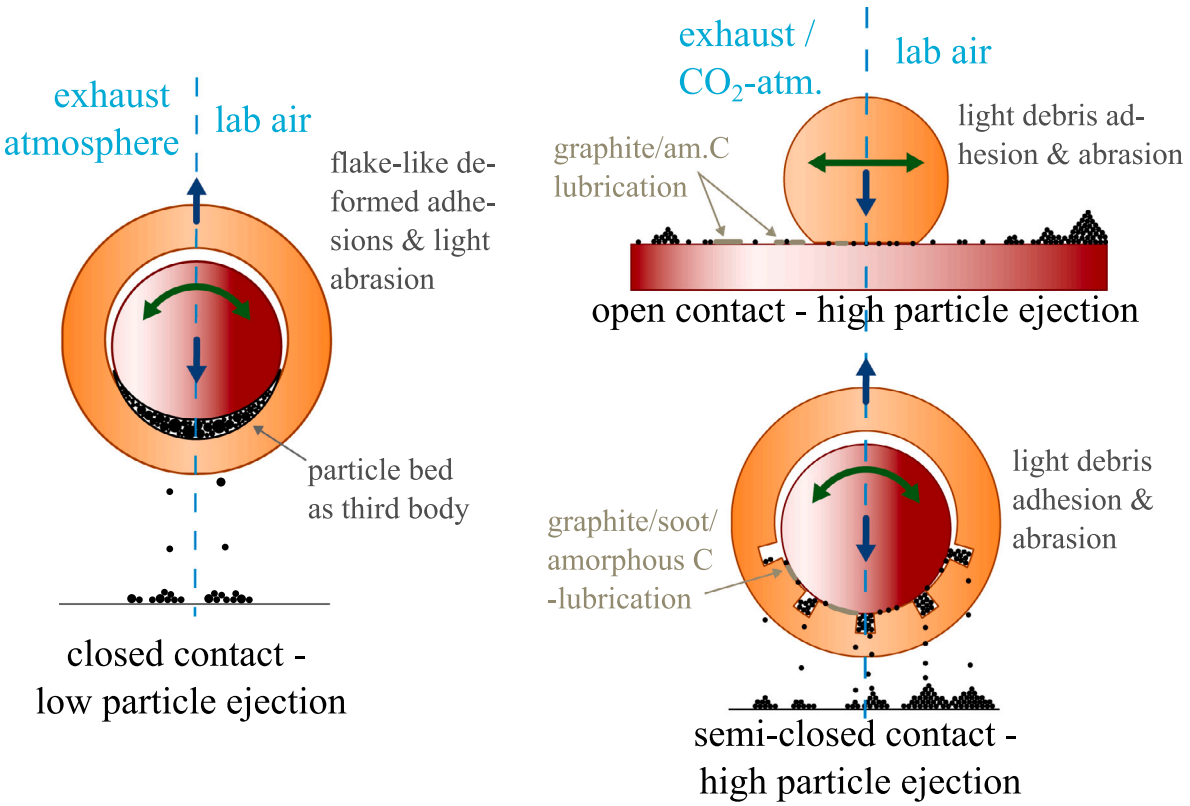

Fig. 27. Comparison of contact geometries with resulting atmosphere dependent tribological mechanisms.

particle ejection, whereas in closed systems this is highly probable, making a more pronounced third body to be expected [22].

However, the length of the possible particle ejection paths should be seen as a decisive factor influencing the formation of a third body [42,56,57]. Baydoun et al. [57] used grooved sample bodies to investigate in depth how different directions of movement in combination with different contact widths affect a fretting contact. It was shown that mainly the particle ejection path in the direction of movement and the displacement δ_0 influence the third body, the path perpendicular to the direction of movement is less important. These results are consistent with the findings of Hintikka et al. [44], who introduce different numbers of slots into a ring-plate contact. The wear increases with decreasing length of the particle ejection path or with an increasing number of slots.

In the field of abrasion, significant differences in wear rates are also known depending on the movement pattern of the abrasive particles [41,47,58–60]. The particles either roll off with a corresponding reduction in wear [48,61,62] or slide with a high level of wear. This change is directly influenced by the mobility of the particles or the contact pressure [59]. When the hard particles roll off, characteristic indents are typically observed [58,59], which were not visible in any of the shaft-bushing tests presented here. Furthermore, very hard particles are used for abrasion tests, whereas the present tests involve wear particles that have a similar oxidation state to the surfaces of the contact bodies. For this reason, it is doubted that the wear-reducing effect of the third body observed here can be explained entirely by a change in the particle movement pattern as found in abrasion tests.

Instead, it is assumed that the different contact geometries are responsible for the differences between the model and system tests. With the grooved bushings, it is clearly shown that not the different contact pressures, but mainly the different particle ejection paths cause the formation of a third body and thus significantly change the wear behaviour. Consequently, in order to maximise the transferability of the test results, the contact geometry from the application should be reproduced in addition to the load and atmospheric conditions (see Fig. 28). Besides contact conformity and opening, particular attention should be placed on comparable particle ejection paths in the direction of movement.

5. Conclusion

This study examines the temperature-dependent tribological behaviour of an austenitic cast iron paired with a hard chromium-plated hot-working steel in a shaft-bushing configuration at temperatures up to 800 °C. By comparing the determined wear characteristics and results with those of a model experiment [6], the **influence of the contact geometry** was evaluated. The following new findings were obtained:

- In the **high temperature** range, a comparable wear behaviour was determined in both experiments, characterised by a wear and friction-reducing glaze layer.
- In the **low temperature** range, differences between the experiments are evident. The model experiment is dominated by the adhesion of the cast iron and slight abrasion. These wear characteristics were also observed on the contact surfaces of the system experiment. But here they are superimposed by a particle bed as a third body, resulting in a wear reduction by a factor of six.
- The geometry-based **formation of a third body** in the system test was prevented and its existence verified with grooved bushings, enabling increased particle ejection. Without third body, significantly higher wear rates were determined, which correspond roughly with the ones of the model experiment.
- **Atmospheric effect:** In the model experiment, a slight reduction in wear and friction was observed in an exhaust gas-like atmosphere. The system experiment showed no changes in exhaust gas compared to tests in air. Again, the grooved bushings

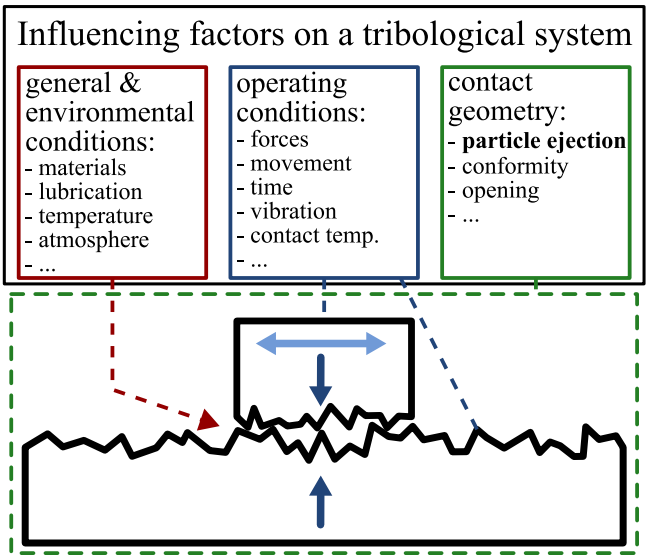

Fig. 28. Influencing factors on a tribological system, categorised into general, environmental and operating conditions, as well as contact geometry.

proved that the third body is responsible for the atmosphere-independent behaviour. Without this particle bed, the same results were achieved as in the model experiment, which were attributed to the lubrication by graphite and soot.

It was demonstrated that the contact geometry and, in particular, the particle ejection have a significant influence on the wear behaviour, the tribological mechanisms and the atmospheric effects. To enable transferable results to the application, comparable contact geometries must be ensured in addition to the general, operating, and environmental conditions (cf. Fig. 28).

CRediT authorship contribution statement

Tobias König: Methodology, Conceptualization, Investigation, Writing – original draft. **Ziping Sang:** Investigation, Writing – review & editing. **Philipp Daum:** Investigation, Writing – review & editing. **Dominik Kürten:** Methodology, Conceptualization, Writing – review & editing, Supervision, Funding acquisition. **Andreas Kailer:** Methodology, Conceptualization, Writing – review & editing, Supervision, Funding acquisition. **Martin Dienwiebel:** Conceptualization, Writing – review & editing, Supervision, Funding acquisition.

Declaration of competing interest

The authors declare the following financial interests/personal relationships which may be considered as potential competing interests: Tobias Koenig reports financial support was provided by Federal Ministry for Economic Affairs and Climate Action. Tobias Koenig reports equipment, drugs, or supplies was provided by Research Association for Combustion Engines. If there are other authors, they declare that they have no known competing financial interests or personal relationships that could have appeared to influence the work reported in this paper.

Acknowledgements

We acknowledge funding from the Federal Ministry for Economic Affairs and Climate of the Federal Republic of Germany under grant agreement no. 21253 N. The authors are grateful for the financial support of AiF (Arbeitsgemeinschaft industrieller Forschungsvereinigungen), Germany within the program for sponsorship by Industrial Joint Research (IGF) of the Federal Ministry for Economic Affairs and Climate Action (BMWK) based on an enactment of the German Parliament. The authors would also like to thank the Forschungsvereinigung Verbrennungsmotoren FVV e.V. for their appreciated technical support.

Appendix A. Supplementary data

Supplementary material related to this article can be found online at https://doi.org/10.1016/j.wear.2025.206001.

References

[1] S. Fouvry, R. Merhej, Introduction of a power law formulation to quantify the contact size effects on friction and wear responses of dry oscillating sliding contacts: Application to a chromium steel interface, Wear 301 (1–2) (2013) 34–46, http://dx.doi.org/10.1016/j.wear.2013.01.072.

[2] A. Dreano, S. Fouvry, G. Guillonneau, Understanding and formalization of the fretting-wear behavior of a cobalt-based alloy at high temperature, Wear 452–453 (2020) 203297, http://dx.doi.org/10.1016/j.wear.2020.203297.

[3] A. Dreano, S. Baydoun, S. Fouvry, S. Nar, P. Alvarez, Influence of a pre-existing glaze layer on the fretting-wear response of HS25 cobalt-based alloy subjected to various temperature conditions, Wear 488–489 (2022) http://dx.doi.org/10.1016/j.wear.2021.204144.

[4] P.H. Shipway, A.M. Kirk, C.J. Bennett, T. Zhu, Understanding and modelling wear rates and mechanisms in fretting via the concept of rate-determining processes - Contact oxygenation, debris formation and debris ejection, Wear 486–487 (2021) 204066, http://dx.doi.org/10.1016/j.wear.2021.204066.

[5] J. Hardell, B. Prakash, High-temperature friction and wear behaviour of different tool steels during sliding against Al–Si-coated high-strength steel, Tribol. Int. 41 (7) (2008) 663–671, http://dx.doi.org/10.1016/j.triboint.2007.07.013.

[6] T. König, T. Kimpel, D. Kürten, A. Kailer, M. Dienwiebel, Influence of atmospheres on the friction and wear of cast iron against chromium plated steel at high temperatures, Wear 522 (2023) 204695, http://dx.doi.org/10.1016/j.wear.2023.204695.

[7] T. Wollmann, S. Nitschke, T. Klauke, T. Behnisch, C. Ebert, R. Füßel, N. Modler, M. Gude, Investigating the friction, wear and damage behaviour of plain bearing bushes of the variable stator vane system, Tribol. Int. 165 (2022) 107280, http://dx.doi.org/10.1016/j.triboint.2021.107280.

[8] K. Meyer, L. Deters, Hochtemperatur-Verschleiß verhalten der Wastegate-Lagerung von Abgasturboladern für Otto-Motoren; Dissertation Univ. Magdeburg, in: Fortschritte in der Maschinenkonstruktion, Shaker-Verl., Aachen, Germany, 2011.

[9] R. van Basshuysen, F. Schäfer (Eds.), Handbuch Verbrennungsmotor: Grundlagen, Komponenten, Systeme, Perspektiven, 8, in: SpringerLink Bücher, Springer Vieweg, Wiesbaden, Germany, 2017, http://dx.doi.org/10.1007/978-3-658-10902-8.

[10] O.A. Zambrano, J.J. Coronado, S.A. Rodríguez, Tempering temperature effect on sliding wear at high temperatures in mottled cast iron, Tribol. Lett. 57 (2) (2015) http://dx.doi.org/10.1007/s11249-014-0462-5.

[11] G. Bolelli, V. Cannillo, L. Lusvarghi, S. Riccò, Mechanical and tribological properties of electrolytic hard chrome and HVOF-sprayed coatings, Surf. Coat. Technol. 200 (9) (2006) 2995–3009, http://dx.doi.org/10.1016/j.surfcoat.2005.04.057.

[12] M.A. Mekicha, M.B. de Rooij, D. Matthews, C. Pelletier, L. Jacobs, D.J. Schipper, The effect of hard chrome plating on iron fines formation, Tribol. Int. 142 (2020) 106003, http://dx.doi.org/10.1016/j.triboint.2019.106003.

[13] B. Podgornik, O. Massler, F. Kafexhiu, M. Sedlacek, Crack density and tribological performance of hard-chrome coatings, Tribol. Int. 121 (182) (2018) 333–340, http://dx.doi.org/10.1016/j.triboint.2018.01.055.

[14] F.P. Bowden, T.P. Hughes, The friction of clean metals and the influence of adsorbed gases. The temperature coefficient of friction, Proc. R. Soc. Lond. Ser. A. Math. Phys. Sci. 172 (949) (1939) 263–279, http://dx.doi.org/10.1098/rspa.1939.0103.

[15] K.-H. Zum Gahr, Microstructure and Wear of Materials, in: Tribology Series, vol. 10, Elsevier, Amsterdam and New York, 2010.

[16] F.H. Stott, High-temperature sliding wear of metals, Tribol. Int. 35 (8) (2002) 489–495, http://dx.doi.org/10.1016/S0301-679X(02)00041-5.

[17] T. Quinn, Oxidational wear, Wear 18 (5) (1971) 413–419, http://dx.doi.org/10.1016/0043-1648(71)90005-6.

[18] F.H. Stott, The role of oxidation in the wear of alloys, Tribol. Int. 31 (1–3) (1998) 61–71, http://dx.doi.org/10.1016/S0301-679X(98)00008-5.

[19] A. Dreano, S. Fouvry, S. Sao-Joao, J. Galipaud, G. Guillonneau, The formation of a cobalt-based glaze layer at high temperature: A layered structure, Wear 440–441 (2019) 203101, http://dx.doi.org/10.1016/j.wear.2019.203101.

[20] C. Rynio, H. Hattendorf, J. Klöwer, G. Eggeler, The evolution of tribolayers during high temperature sliding wear, Wear 315 (1–2) (2014) 1–10, http://dx.doi.org/10.1016/j.wear.2014.03.007.

[21] M. Godet, The third-body approach: A mechanical view of wear, Wear 100 (1–3) (1984) 437–452, http://dx.doi.org/10.1016/0043-1648(84)90025-5.

[22] M. Godet, Third-bodies in tribology, Wear 136 (1) (1990) 29–45, http://dx.doi.org/10.1016/0043-1648(90)90070-Q.

[23] S. Descartes, Y. Berthier, Rheology and flows of solid third bodies: background and application to an MoS1.6 coating, Wear 252 (7–8) (2002) 546–556, http://dx.doi.org/10.1016/S0043-1648(02)00008-X.

[24] N. Fillot, I. Iordanoff, Y. Berthier, Wear modeling and the third body concept, Wear 262 (7–8) (2007) 949–957, http://dx.doi.org/10.1016/j.wear.2006.10.011.

[25] G.P. Merker, Grundlagen Verbrennungsmotoren: Funktionsweise, Simulation, Messtechnik, seventh ed., ATZ/MTZ-Fachbuch Ser, Springer Fachmedien Wiesbaden GmbH, Wiesbaden, 2014, http://dx.doi.org/10.1007/978-3-658-03195-4.

[26] M.S. Rahman, J. Ding, A. Beheshti, X. Zhang, A.A. Polycarpou, Helium tribology of inconel 617 at elevated temperatures up to 950°C: Parametric study, Nucl. Sci. Eng. 193 (9) (2019) 998–1012, http://dx.doi.org/10.1080/00295639.2019.1582315.

[27] I. Velkavrh, F. Ausserer, S. Klien, J. Brenner, P. Forêt, A. Diem, The effect of gaseous atmospheres on friction and wear of steel–steel contacts, Tribol. Int. 79 (2014) 99–110, http://dx.doi.org/10.1016/j.triboint.2014.05.027.

[28] I. Velkavrh, F. Ausserer, S. Klien, J. Voyer, A. Ristow, J. Brenner, P. Forêt, A. Diem, The influence of temperature on friction and wear of unlubricated steel/steel contacts in different gaseous atmospheres, Tribol. Int. 98 (2016) 155–171, http://dx.doi.org/10.1016/j.triboint.2016.02.022.

[29] M. Esteves, A. Ramalho, F. Ramos, Fretting behavior of the AISI 304 stainless steel under different atmosphere environments, Tribol. Int. 88 (J6) (2015) 56–65, http://dx.doi.org/10.1016/j.triboint.2015.02.016.

[30] M. Qiu, L. Chen, Tribological characteristics of chromium steels in three various atmospheres under high-speed conditions, Wear 268 (11–12) (2010) 1342–1346, http://dx.doi.org/10.1016/j.wear.2010.02.006.

[31] Deutsches Institut für Normung e. V., DIN 4957: Werkzeugstähle, Beuth Verlag GmbH, Berlin, Germany, 2018, http://dx.doi.org/10.31030/2842661.

[32] Deutsches Institut für Normung e. V., DIN EN 13835: Gießereiwesen - Austenitische Gusseisen, Beuth Verlag GmbH, Berlin, Germany, 2012, http://dx.doi.org/10.31030/1809755.

[33] I. Llavori, A. Zabala, A. Aginagalde, W. Tato, J.J. Ayerdi, X. Gómez, Critical analysis of coefficient of friction derivation methods for fretting under gross slip regime, Tribol. Int. 143 (2020) 105988, http://dx.doi.org/10.1016/j.triboint.2019.105988.

[34] X. Jin, W. Sun, P.H. Shipway, Derivation of a wear scar geometry-independent coefficient of friction from fretting loops exhibiting non-Coulomb frictional behaviour, Tribol. Int. 102 (2016) 561–568, http://dx.doi.org/10.1016/j.triboint.2016.06.012.

[35] ASTM Committee G02, Guide for Determining Friction Energy Dissipation in Reciprocating Tribosystems: G0203-10, ASTM International, West Conshohocken, USA, 2016, http://dx.doi.org/10.1520/G0203-10R16.

[36] Lloyd Twaites, in: RRUFF Database (Ed.), Name: Magnetite; RRUFF ID: R060191; Unpolarized 532nm Laser, Tuscon, Arizona and USA, 2006.

[37] University of Arizona Mineral Museum 12904, in: RRUFF Database (Ed.), Name: Hematite; RRUFF ID: R040024; Unpolarized 532nm Laser, Tuscon, Arizona and USA, 1988.

[38] L. Monaco, R.N. Sodhi, G. Palumbo, U. Erb, XPS study on the passivity of coarse-grained polycrystalline and electrodeposited nanocrystalline nickel-iron (NiFe) alloys, Corros. Sci. 176 (2020) 108902, http://dx.doi.org/10.1016/j.corsci.2020.108902.

[39] A. Machet, A. Galtayries, P. Marcus, P. Combrade, P. Jolivet, P. Scott, XPS study of oxides formed on nickel–base alloys in high–temperature and high–pressure water, Surf. Interface Anal. 34 (1) (2002) 197–200, http://dx.doi.org/10.1002/sia.1282.

[40] C.E. Morstein, M. Dienwiebel, Graphite lubrication mechanisms under high mechanical load, Wear 477 (2021) 203794, http://dx.doi.org/10.1016/j.wear.2021.203794.

[41] D. Grasser, S. Corujeira Gallo, M. Pereira, M. Barnett, Experimental investigation of the effect of insert spacing on abrasion wear resistance of a composite, Wear 494–495 (2022) 204277, http://dx.doi.org/10.1016/j.wear.2022.204277.

[42] J. Aleksejev, Z. Clark, J.E. Huber, Da Hills, Experimental investigation of debris entrapment in annular contacts, Proc. Inst. Mech. Eng. Part J: J. Eng. Tribol. 235 (4) (2021) 687–697, http://dx.doi.org/10.1177/1350650120910670.

[43] T.J. Hakala, A. Laukkanen, T. Suhonen, K. Holmberg, A finite-element model for a paste lubricated steel wire vs cast iron contact, Tribol. Int. 150 (2020) 106362, http://dx.doi.org/10.1016/j.triboint.2020.106362.

[44] J. Hintikka, A. Lehtovaara, A. Mäntylä, Third particle ejection effects on wear with quenched and tempered steel fretting contact, Tribol. Trans. 60 (1) (2017) 70–78, http://dx.doi.org/10.1080/10402004.2016.1146813.

[45] Z. Lin, B. Gao, X. Li, K. Yu, Effect of abrasive grain size on surface particle deposition behaviour of PTFE/bronze composites during abrasive wear, Tribol. Int. 139 (2019) 12–21, http://dx.doi.org/10.1016/j.triboint.2019.06.027.

[46] R. Gåhlin, S. Jacobson, The particle size effect in abrasion studied by controlled abrasive surfaces, Wear 224 (1) (1999) 118–125, http://dx.doi.org/10.1016/S0043-1648(98)00344-5.

[47] D. Grasser, S. Corujeira Gallo, M.P. Pereira, M. Barnett, Wear simulation and validation of composites (insert-reinforced matrix) in the dry sand rubber wheel test, Miner. Eng. 207 (2024) 108583, http://dx.doi.org/10.1016/j.mineng.2024.108583.

[48] I.M. Hutchings, Mechanisms of wear in powder technology: A review, Powder Technol. 76 (1) (1993) 3–13, http://dx.doi.org/10.1016/0032-5910(93)80035-9.

[49] J.M. Shockley, S. Descartes, E. Irissou, J.-G. Legoux, R.R. Chromik, Third body behavior during dry sliding of cold-sprayed Al-Al2O3 composites: In situ tribometry and microanalysis, Tribol. Lett. 54 (2) (2014) 191–206, http://dx.doi.org/10.1007/s11249-014-0326-z.

[50] M.M. de Oliveira, H.L. Costa, W.M. Silva, J. de Mello, Effect of iron oxide debris on the reciprocating sliding wear of tool steels, Wear 426–427 (2019) 1065–1075, http://dx.doi.org/10.1016/j.wear.2018.12.047.

[51] O. Bouillanne, G. Mollon, A. Saulot, S. Descartes, N. Serres, G. Chassaing, K. Demmou, How vorticity and agglomeration control shear strength in soft cohesive granular flows, Granul. Matter 24 (2) (2022) http://dx.doi.org/10.1007/s10035-022-01216-8.

[52] O. Bouillanne, G. Mollon, A. Saulot, S. Descartes, N. Serres, G. Chassaing, K. Demmou, Wear in progress: How third body flow controls surface damage, Tribol. Lett. 72 (3) (2024) 84, http://dx.doi.org/10.1007/s11249-024-01875-z.

[53] Y. Zhang, G. Mollon, S. Descartes, Significance of third body rheology in friction at a dry sliding interface observed by a multibody meshfree model: Influence of cohesion between particles, Tribol. Int. 145 (2020) 106188, http://dx.doi.org/10.1016/j.triboint.2020.106188.

[54] H.L. Costa, M.M. Oliveira Jr., J. de Mello, Effect of debris size on the reciprocating sliding wear of aluminium, Wear 376–377 (2017) 1399–1410, http://dx.doi.org/10.1016/j.wear.2016.10.025.

[55] A. Iwabuchi, H. Kubosawa, K. Hori, The dependence of the transition from severe to mild wear on load and surface roughness when the oxide particles are supplied before sliding, Wear 139 (2) (1990) 319–333, http://dx.doi.org/10.1016/0043-1648(90)90054-E.

[56] G. Colas, A. Saulot, C. Godeau, Y. Michel, Y. Berthier, Decrypting third body flows to solve dry lubrication issue – MoS2 case study under ultrahigh vacuum, Wear 305 (1–2) (2013) 192–204, http://dx.doi.org/10.1016/j.wear.2013.06.007.

[57] S. Baydoun, S. Fouvry, S. Descartes, Modeling contact size effect on fretting wear: a combined contact oxygenation - third body approach, Wear 488–489 (2022) 204168, http://dx.doi.org/10.1016/j.wear.2021.204168.

[58] J.C. Poletto, P.D. Neis, D. Fauconnier, A. Ramalho, P. de Baets, N.F. Ferreira, A systematic investigation of grooving and rolling abrasive mechanisms using surface topography, Wear 548–549 (2024) 205389, http://dx.doi.org/10.1016/j.wear.2024.205389.

[59] R.C. Cozza, Effect of sliding distance on abrasive wear modes transition, J. Mater. Res. Technol. 4 (2) (2015) 144–150, http://dx.doi.org/10.1016/j.jmrt.2014.10.007.

[60] L. Fang, X.L. Kong, J.Y. Su, Q.D. Zhou, Movement patterns of abrasive particles in three-body abrasion, Wear 162–164 (1993) 782–789, http://dx.doi.org/10.1016/0043-1648(93)90079-2.

[61] J. Tong, T.-b. Lü, Y.-h. Ma, H.-k. Wang, L.-q. Ren, R.D. Arnell, Two-body abrasive wear of the surfaces of Pangolin scales, J. Bionic Eng. 4 (2) (2007) 77–84, http://dx.doi.org/10.1016/S1672-6529(07)60017-1.

[62] E. Rabinowicz, L.A. Dunn, P.G. Russell, A study of abrasive wear under three-body conditions, Wear 4 (5) (1961) 345–355, http://dx.doi.org/10.1016/0043-1648(61)90002-3.